

# Assessment and prediction of dust emissions, deposition and radiation forcing in Central Asia

Ying Gan<sup>123</sup>, Zhe Zhang<sup>1234\*</sup>, Wen Chu<sup>5</sup>, Jianli Ding<sup>6</sup>, Yuxin Ren<sup>123</sup>

<sup>1</sup>College of Geography and Remote Sensing Sciences, Xinjiang University, Urumqi, 830046, China

<sup>2</sup>Xinjiang Key Laboratory of Oasis Ecology, Xinjiang University, Urumqi, 830046, China

<sup>3</sup>Key Laboratory of Smart City and Environment Modelling of Higher Education Institute, Xinjiang University, Urumqi, 830046, China

<sup>4</sup>MNR Technology Innovation Center for Central Asia Geo-Information Exploitation and Utilization, Urumqi, 830046, China

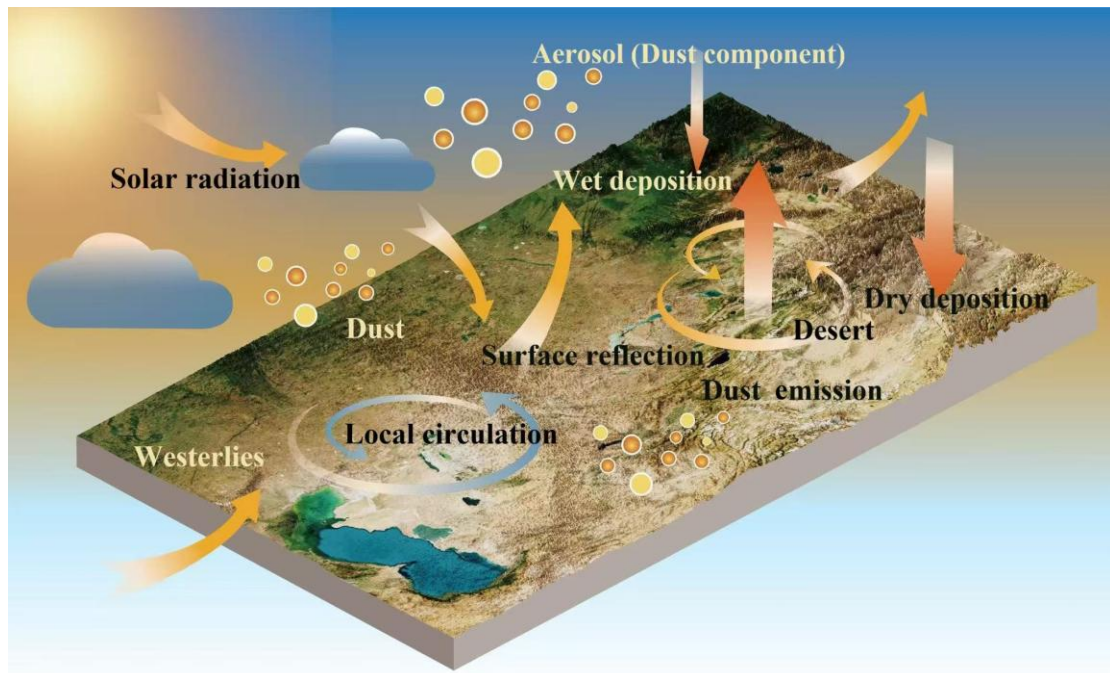
<sup>5</sup>College of Marine Technology, Faculty of Information Science and Engineering, Ocean University of China; Qingdao, 266100

<sup>6</sup>Xinjiang Institute of Technology, Aksu, China;

\*Correspondence to: zhangzhe\_0110@yeah.net; Tel: +86 18799181249

**Abstract.** Dust aerosols significantly influence climate by modulating radiative balance and cloud processes. This study integrates MERRA-2 reanalysis data and the CMIP6 multi-model ensemble to assess the spatiotemporal evolution of dust emissions, deposition, and associated radiative effects in Central Asia from 1980 to 2100. Four SSP scenarios project that dust emissions in Central Asia exhibit a high-emission, high-deposition pattern with primary sources exceeding  $15 \mu\text{g}\cdot\text{m}^{-2}\cdot\text{s}^{-1}$ . The deposition area substantially exceeds the source area (maximum  $>8 \mu\text{g}\cdot\text{m}^{-2}\cdot\text{s}^{-1}$ ). Cross-scenario analysis demonstrates that dust emissions are highly sensitive to climate policy, with end-of-century emissions in the SSP5-8.5 high-emission scenario increasing by 94.9% relative to the baseline period. In contrast, emissions under the SSP1-2.6 low-carbon pathway vary by only 4.5%. Simulations using the SBDART model show that aerosol direct radiative forcing (ADRF) from dust in Central Asia under clear-sky conditions exhibits a vertical gradient, with cooling at the top of the atmosphere (TOA) and heating near the surface, yielding a net negative forcing at the TOA, with a minimum of  $<-10 \text{ W/m}^2$  near the Caspian Sea. Peak positive forcing within the atmosphere, observed in spring, reaches  $10.0 \text{ W/m}^2$ . Increased dust emissions reduce shortwave radiation at the surface by up to  $-20 \text{ W/m}^2$ . Ground-based observations indicate seasonal variations in the dust-induced heating rate, with peak radiative forcing in spring at Kashgar ( $93.0 \text{ W/m}^2$ ) and a maximum near-surface heating rate of  $2.6 \text{ K/day}$ . In contrast, the near-surface heating rate at Issyk-Kul Lake in autumn ( $0.34 \text{ K/day}$ ) is approximately four times higher than in spring ( $0.08 \text{ K/day}$ ).

32 **Graphical Abstract**



33

34 **Keywords:** Dust cycle; CMIP6 multi-model ensemble(MME); Direct radiative forcing of dust;  
35 SBDART model

36 **1.Introduction**

37 Dust aerosols are a significant component of the tropospheric aerosol mass load, accounting for  
38 approximately 50%, and profoundly impact the functioning of the Earth system (Mahowald et al., 2010;  
39 Ramanathan et al., 2001). Their transboundary circulation process (lithosphere-atmosphere-cryosphere)  
40 and interaction with the climate system have become cutting-edge research areas in Earth system science.  
41 The release, transport, and deposition of dust aerosols not only involve multiple geospheres but also  
42 substantially affect weather, climate, air quality, and human health upon entering the atmosphere (Tegen  
43 et al., 2004; Penner et al., 2006; Pozzer et al., 2012).

44 Global annual dust emissions are substantial, ranging from approximately 1000 to 2150 Tg, with 30%  
45 to 40% originating from arid regions of Asia (Tanaka & Chiba, 2006). Dust is transported across  
46 continents by westerly wind circulation, significantly influencing the atmospheric radiation balance in  
47 East Asia, North America, and the Arctic region (Wallace & Hobbs, 2006). Although studies have  
48 confirmed that dust regulates the land-atmosphere energy budget through direct radiative forcing  
49 (including scattering and absorption of shortwave and longwave radiation) and indirect effects (such as

50 altering precipitation efficiency as cloud condensation nuclei), significant uncertainty persists regarding  
51 the vertical distribution of dust, the amplification mechanism of anthropogenic emissions, and their  
52 regional climate feedback (IPCC, 2021).

53 Due to the challenges associated with dust observation, our understanding of the behavior of dust  
54 throughout its life cycle remains insufficient, hindering a complete understanding and accurate modeling  
55 of its complex mechanism of action (Kok et al. 2023, Rupakheti et al. 2023). Numerous studies have  
56 used a variety of methods, including in situ observations, satellite remote sensing, and model simulations,  
57 to thoroughly examine the spatiotemporal changes, optical properties, and radiative forcing of dust  
58 aerosols(Wang et al. 2018, Song et al. 2021, Chen, Zhao and Fan 2022). For example, global dust is  
59 primarily confined to the "dust belt," with approximately one-third originating from the Asian  
60 region(Kok et al. 2023). Dai et al. utilized a variety of remote sensing and ground-based data to study  
61 the sources, microphysical characteristics, and optical properties (Dai et al. 2022, Salvador et al. 2022).

62 Zhao et al. investigated the simulation of global and regional dust by 16 CMIP6 models in the  
63 Atmospheric Model Intercomparison Project (AMIP) experiment and compared the results with  
64 observational and reanalysis data (Zhao et al. 2023, Liu et al. 2024).

65 Model simulations provide information on the temporal and spatial changes of dust aerosols worldwide  
66 and facilitate predictions of future trends (Li et al., 2021). Climate models, such as CMIP5 and CMIP6,  
67 have enhanced our understanding of the main characteristics of dust aerosols. These models feature  
68 increasing resolutions and increasingly complex physical processes and parameterizations,  
69 demonstrating their ability to simulate dust events and processes on meso- to global scales (Zhao et al.,  
70 2022). In particular, CMIP6 experiments have provided critical support for assessing the climatic effects  
71 of dust emissions (Braconnot et al., 2021; Zhao et al., 2024). However, due to insufficient resolution and  
72 simplified regional topography, the applicability of these global studies to the arid regions of Central  
73 Asia remains limited, underscoring the need for high-resolution analyses at the regional scale.

74 The arid regions of Central Asia, including Xinjiang in China, constitute the world's second-largest dust  
75 source area, with distinctive surface characteristics leading to significant spatiotemporal variations in  
76 dust emission fluxes (Shen et al., 2016). However, current research has primarily focused on the  
77 spatiotemporal distribution and transport processes of dust (Li et al., 2022b; Tao et al., 2022), while key  
78 aspects of the local dust lifecycle in this region—such as the long-term evolution of dust emission—

79 deposition budgets, the strong dependence of direct radiative forcing on dust vertical profiles, and modal  
80 differences in dust–climate feedbacks under different carbon emission scenarios—remain poorly  
81 understood. These knowledge gaps significantly constrain the reliability of climate models over Central  
82 Asia, and uncertainties in radiative forcing estimates primarily stem from the lack of ground-based  
83 validation due to the scarcity of observational stations (Brown et al., 2021; Wu & Boor, 2021).

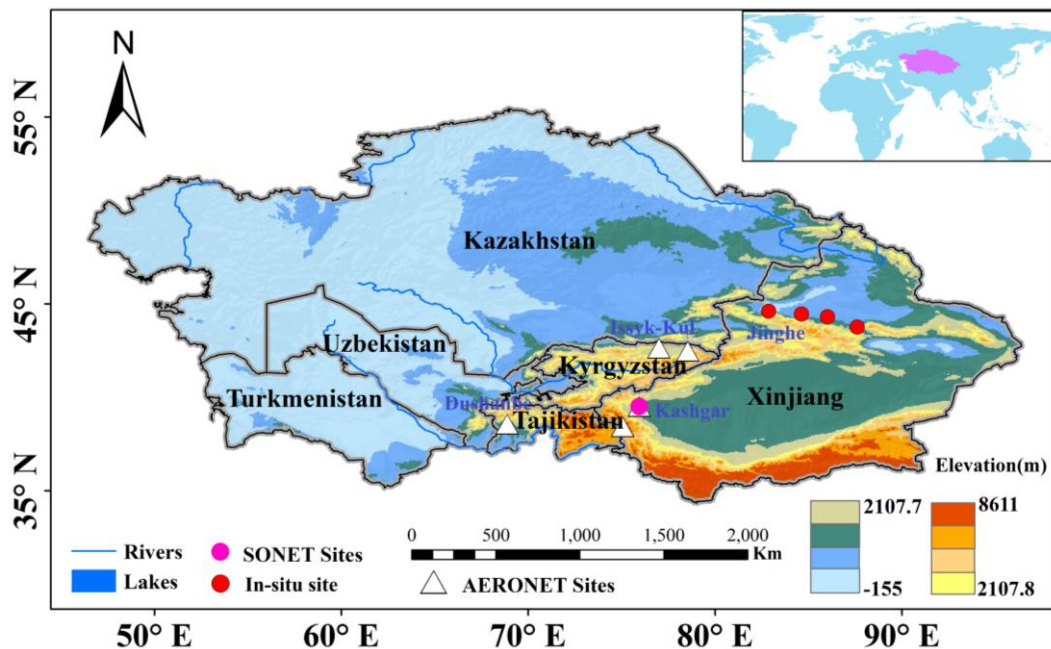
84 To overcome the above limitations, this study establishes a multi-source data integration framework that  
85 systematically incorporates a full-chain analysis of “emission–deposition–radiation,” focusing on the  
86 regional characteristics of the dust lifecycle over the arid regions of Central Asia. Unlike previous studies  
87 that have mainly concentrated on the global scale (Kok et al., 2023; Zhao et al., 2022, 2023, 2024), this  
88 work achieves an integrated assessment at the regional scale and emphasizes the role of observations in  
89 constraining model uncertainties. The specific innovations are reflected in three aspects: (1) by  
90 combining MERRA-2 reanalysis with CMIP6 multi-model ensembles through statistical downscaling,  
91 the long-term evolution of dust emission–deposition budgets and their scenario-based differences in  
92 Central Asia are systematically characterized, thereby providing regionally refined insights to  
93 complement global model results; (2) using the SBDART radiative transfer model together with  
94 observational data from the SONET Asian Dust Monitoring Network and the Jinghe CE318 ground-  
95 based remote sensing site, the long-term trends of dust shortwave radiative forcing under clear-sky  
96 conditions are quantified; and (3) by introducing the SARIMA statistical model, the short-term evolution  
97 and risk implications of dust radiative effects are explored. This framework not only deepens the  
98 understanding of dust physical mechanisms under the complex topography and local climate of Central  
99 Asia but also provides new scientific support for improving regional climate simulations and  
100 environmental risk management.

101 The structure of this paper is as follows. Section 2 presents the data sources, the downscaling method for  
102 the CMIP6 dust budget, and the calculation method for clear-sky aerosol radiative forcing. Section 3  
103 examines the detailed characteristics of the dust budget, projections of future changes, and the radiative  
104 forcing of dust aerosols. Finally, the main conclusions and a discussion are presented in Section 4.

105 **2. Data and Methods**

106 **2.1 Data sources**

107 The study area is situated between 35°–57°N and 48°–96°E, encompassing the five Central Asian  
108 countries (Kazakhstan, Uzbekistan, Tajikistan, Turkmenistan, and Kyrgyzstan) and the Xinjiang region  
109 of China (comprising both its northern and southern parts). This region, located in the hinterland of the  
110 Eurasian continent, is characterized by a temperate continental climate with extreme aridity. The region  
111 features a highly heterogeneous surface, with the Taklamakan Desert and the surrounding Gobi  
112 (comprising over 40% of the study area) interspersed with mountain ranges, such as the Tianshan and  
113 Pamir, forming a unique landform (Shen et al., 2016; Hetzel et al., 2002). As the world’s second-largest  
114 source of dust, strong thermal and dynamic coupling drives intense dust activities (Zhang et al., 2020),  
115 with emission hotspots concentrated in the Tarim Basin, the desiccated bed of the Aral Sea, and the  
116 Kazakh steppe belt. This study focuses on the regional dust budget and radiative effects, utilizing  
117 MERRA-2 reanalysis data, the CMIP6 multi-model ensemble, AERONET, SONET, and handheld  
118 photometer data.



119  
120 **Figure. 1 Location of the Study area.**

121 **2.1.1 Ground-based sun photometer data**

122 AERONET (Aerosol RObotic NETwork) employs a CE-318 solar photometer to measure aerosol optical

123 depth (AOD) across eight bands in the range of 340–1640 nm and to derive microphysical parameters,  
124 including single scattering albedo (SSA), refractive index ( $m$ ), and particle size spectrum (Holben et al.,  
125 1998; Holben et al., 2001). The Level 2 data exhibit an uncertainty of less than 5%. As an internationally  
126 recognized standard for ground-based aerosol observations, its long-term stability and algorithmic  
127 consistency provide reliable input for radiative forcing calculations (García et al., 2012). The data used  
128 in this study are available from the AERONET website (<https://aeronet.gsfc.nasa.gov/>).

129 The Chinese Academy of Sciences-led SONET (Sun-sky radiometer Observation NETwork) employs  
130 the CE318-DP instrument to provide information on the chemical composition and vertical profile of  
131 aerosols while adhering to AERONET’s stringent quality control procedures. The establishment of  
132 SONET sites has effectively addressed gaps in AERONET’s spatial coverage in this source region (Li et  
133 al., 2018). Cross-validation demonstrates that the correlation coefficient between SONET and  
134 AERONET AOD is 0.98 (RMSE < 0.02), confirming a seamless integration of the two datasets (She et  
135 al., 2024). The SONET data can be accessed from its official website (<http://www.sonet.ac.cn/>).

136 To supplement the limited temporal and spatial coverage of fixed stations, this study employs CE-318  
137 and Microtops II handheld photometers to obtain transient AOD observations in the 550–870 nm band  
138 (accuracy  $\pm 0.01$ ) for verifying the local applicability of satellite inversion products. By integrating these  
139 multi-scale observational data, this study uses AERONET and SONET Level 2 data to provide vertical  
140 profiles of aerosol optical-physical properties, calculate the direct radiative forcing of aerosols, and  
141 validate satellite data on AOD and radiation flux in Central Asia (Supplementary Figure 1).

### 142 **2.1.2 MERRA-2 reanalysis data**

143 The MERRA-2 reanalysis data used in this study was developed by NASA’s Goddard Space Flight  
144 Center. Its core is based on the GEOS-5 atmospheric circulation model and the ADAS-5.12.4  
145 assimilation system. A global multi-element dataset with 72 vertical layers (surface to 80 km) and a  
146 horizontal resolution of  $0.625^\circ \times 0.5^\circ$  has been constructed from 1980 to the present by integrating satellite  
147 remote sensing (MODIS/AVHRR aerosol optical thickness), ground-based observations (soundings,  
148 aircraft observations), and GOCART aerosol chemical transport model output (Gelaro et al., 2017). In  
149 addition to covering variables related to clouds, radiation, and hydrological cycles, the coupled GOCART  
150 model distinguishes the interaction mechanisms of five aerosol types in this dataset: dust (DU), sea salt

151 (SS), sulfate (SO<sub>4</sub>), black carbon (BC), and organic carbon (OC). For the first time, the entire lifecycle  
 152 of dust aerosols has been analyzed, providing key parameters such as monthly average dust emission  
 153 flux, dry/wet deposition rate, particle size-classified loads, and single scattering albedo at 483.5 nm,  
 154 ensuring physical consistency for quantifying dust radiative forcing (Buchard et al., 2017). Leveraging  
 155 these data advantages, this study extracts radiation flux and dust cycle parameters under clear-sky  
 156 conditions in Central Asia and systematically constructs a collaborative analysis framework for dust  
 157 emissions, deposition, and radiative forcing.

### 158 2.1.3 CMIP6 model simulations

159 The Sixth Coupled Model Intercomparison Project (CMIP6) incorporates 112 climate models from 33  
 160 institutions worldwide, with its multi-scenario simulations substantially exceeding those of previous  
 161 studies in both breadth and depth (Eyring et al., 2016). To examine the decadal variations in dust  
 162 emissions and dry and wet deposition in Central Asia, this study selected ten models from CMIP6 based  
 163 on data completeness (Eyring et al., 2016). The selection criteria encompassed key variables in the dust  
 164 cycle: monthly mean dust emission fluxes for the historical period (1980–2014) and for four Shared  
 165 Socioeconomic Pathways (SSP1-2.6, SSP2-4.5, SSP3-7.0, and SSP5-8.5) from 2015 to 2100, as well as  
 166 dust dry- and wet-deposition fluxes (the sum of which constitutes total deposition).

167 To ensure spatial consistency when comparing multi-source data, all model outputs were statistically  
 168 downscaled and regridded to match the MERRA-2 reanalysis data (spatial resolution: 0.625° × 0.5°).  
 169 This multi-model ensemble approach effectively captures uncertainties in climate responses while  
 170 managing computational costs, thereby providing robust data support for analyzing the long-term  
 171 evolution of the dust cycle in the arid region of Central Asia.

172 **Table.1 Overview of the models and simulations used in this study.**

<b>Model</b>	<b>Nation</b>	<b>Resolution</b>	<b>Hist</b>	<b>SSP126</b>	<b>SSP245</b>	<b>SSP370</b>	<b>SSP585</b>	<b>Dust emission scheme</b>	<b>Model references</b>
CESM2-WACCM	USA	1.25°×0.94°	3	1	5	3	5	Zender et al. (2003)	Danabasoglu et al. (2020)
CESM2	USA	1.25°×0.95°	11	3	3	3	3	Zender et al. (2003)	Wu et al. (2016)

CNRM-ESM2-1	France	1.25°×0.96°	3	5	10	5	5	Marticorena et al. (1997)	Séférian et al. (2019)
GFDL-ESM4	USA	1.25°×0.97°	1	1	1	1	1	Evans et al. (2016)	Dunne et al. (2020)
GISS-E2-1-G	USA	1.25°×0.98°	19	10	25	17	10	Ginoux et al. (2004)	Bauer et al. (2020)
GISS-E2-1-H	USA	1.25°×0.99°	10	5	5	1	5	Bauer and Koch.(2005)	Kelley et al. (2020)
GISS-E2-2-G	USA	1.25°×1.00°	5	5	5	5	5	Cakmur et al. (2006)	Rind et al. (2020)
MRI-ESM2-0	Japan	1.25°×1.01°	12	5	10	5	6	Tanaka and Chiba.(2005)	Yukimoto et al. (2019)
HadGEM3-GC31-LL	UK	1.875°×1.25°	5	3	4	2	3	Marticorena. (1995)	Williams et al. (2020)
UKESM1-0-LL	UK	1.25°×0.103°	3	5	5	3	4	Marticorena. (1995)	Senior et al. (2020)

## 173 2.2 Methodology

### 174 2.2.1 Delta statistical downscaling

175 Due to the limited original spatial resolution of the CMIP6 models (typically  $\sim 1.25^\circ \times 1^\circ$ ), their direct  
176 application to regional-scale dust cycle analyses may introduce systematic biases. Therefore, this study  
177 employs the delta change factor method for statistical downscaling. At its core, this method separates the  
178 historical biases of the climate models from the future change signal, enabling the reconstruction of high-  
179 resolution climate variables (Maraun et al., 2010; Gutmann et al., 2014).

180 First, deviations during the baseline period are calculated by extracting the monthly mean dust emission  
181 fluxes,  $P_{m,his}$ , from the historical simulations (1980–2014) of each CMIP6 model. These fluxes are then  
182 matched to the MERRA-2 reanalysis observations,  $P_{obs}$ , for the same period to determine the model's  
183 systematic deviation ratio.

$$184 \quad B_m = \frac{P_{m,his}}{P_{obs}} \quad (1)$$

185 where  $\overline{P_{obs}}$  is the monthly average of the observation period, and  $Bm$  represents the spatial deviation of  
186 model  $m$  in the reference period.

187 Second, the relative change factor for future scenarios is extracted, and the ratio of dust emissions for  
188 each model during the future scenario period (2015–2100) relative to its historical simulation is

189 calculated.

$$190 \quad R_{m,fut} = \frac{P_{m,fut}}{P_{m,his}} \quad (2)$$

191 Among them,  $P_{m,fut}$  is the monthly mean emission of model  $m$  in the future, and  $P_{m,his}$  is the monthly  
192 mean emission of model  $m$  over the historical period.

193 This approach decouples the historical deviations from the climate change signal, preserving the physical  
194 response characteristics of CMIP6 to future climate forcings while enhancing simulation accuracy at the  
195 regional scale through the incorporation of high-resolution observational data. Compared to dynamic  
196 downscaling, it substantially reduces computational costs and is particularly suitable for multi-model  
197 uncertainty quantification studies.

### 198 **2.2.2 SBDART Radiative Transfer Model Calculation of Direct Radiative Forcing of Aerosols**

199 The Santa Barbara DISORT Atmospheric Radiative Transfer (SBDART) model (Ricchiuzzi et al., 1998)  
200 was employed in this study to quantitatively assess the direct radiative effects of aerosols. SBDART  
201 solves the atmospheric radiative transfer equation using the four-stream approximation. Its core  
202 architecture comprises three modules: first, the discrete ordinates radiative transfer (DISORT) module,  
203 which calculates the radiative fluxes in a 45-layer atmosphere (with a vertical resolution of 0.3 km);  
204 second, the spectral parameterization module, which integrates the LOWTRAN-7 atmospheric  
205 absorption spectrum and Mie scattering theory to cover the shortwave band from 0.25 to 4.0  $\mu\text{m}$ ; and  
206 third, the surface-atmosphere coupling module, which analyzes the radiative interactions between surface  
207 albedo and atmospheric constituents such as water vapor and ozone.

208 This study is based on a comprehensive dataset, with key input parameters including the optical  
209 properties (e.g., optical depth  $\tau$ , single scattering albedo  $\omega$ , asymmetry factor  $g$ ) and the vertical profiles  
210 of aerosols. These parameters were obtained from the solar photometer observation network in Central  
211 Asia, which provides significant advantages in temporal and spatial resolution compared to satellite  
212 retrieval products (Dubovik & King, 2000). To quantify the radiative forcing due to dust aerosols, all  
213 simulations were conducted under clear-sky conditions, with the solar zenith angle fixed to the seasonal  
214 mean value for the study area to ensure the comparability of regional radiative effects (Halothore et al.,  
215 2005). The aerosol direct radiative forcing (ADRF) was calculated using the standard approach, which  
216 determines the difference in net radiative flux with and without aerosols under cloud-free conditions.

217 Specifically, the ADRF at a given altitude  $z$ , at the top of the atmosphere (TOA), at the surface (SFC),  
 218 and in the atmosphere (ATM) can be defined as follows:

$$219 \quad NF_z = F_{z,down} - F_{z,up} \quad (3)$$

$$220 \quad ADRF_z = NF_z^{aer} - NF_z^{noaer} \quad (4)$$

$$221 \quad ADRF_{TOA} = NF_{TOA}^{aer} - NF_{TOA}^{noaer} \quad (5)$$

$$222 \quad ADRF_{SFC} = NF_{SFC}^{aer} - NF_{SFC}^{noaer} \quad (6)$$

$$223 \quad ADRF_{ATM} = ADRF_{TOA} - ADRF_{SFC} \quad (7)$$

$$224 \quad ADRF_{dust} = ADRF \times \left( \frac{DAOD}{AOD} \right) \quad (8)$$

225 Among them,  $F_{z,down}$  and  $F_{z,up}$  are the downward and upward radiative fluxes,  $NF_z^{aer}$  and  $NF_z^{noaer}$  are  
 226 the net radiative fluxes with and without aerosols, and ADRF is the aerosol direct radiative forcing.

### 227 **2.2.3 SARIMA prediction model**

228 Given the non-stationarity and interannual cycle characteristics of the radiative forcing time series of  
 229 Central Asian dust, this study employs the seasonal autoregressive integrated moving average (SARIMA)  
 230 model for analysis. First, the augmented Dickey-Fuller test (ADF,  $p < 0.05$ ) was used to confirm the non-  
 231 stationarity of the series. A compound differencing strategy (first-order conventional difference  $d=1$ ,  
 232 first-order seasonal difference  $D=1$ , period  $s=12$ ) was applied to eliminate trend and interannual  
 233 fluctuations, resulting in a stationary residual series (KPSS test,  $p > 0.1$ ).

234 The non-seasonal order ( $p=2$ ,  $q=1$ ) was determined based on the autocorrelation function (ACF) and  
 235 partial autocorrelation function (PACF), while the seasonal order ( $P=1$ ,  $Q=1$ ) was optimized using grid  
 236 search, yielding the final SARIMA(2,1,1)(1,1,1)<sub>12</sub> model (AIC=112.3, BIC=125.7). Model validation  
 237 demonstrated a goodness of fit of  $R^2=0.87$  for annual cycle dynamics, with a prediction error for extreme  
 238 event peaks of less than 15%, confirming its effectiveness in analyzing non-stationary sequences (Sirisha  
 239 et al., 2022).

### 240 **2.2.4 Linear Trend Method**

241 In this study, the ordinary least squares (OLS) method was used to perform linear regression on the dust  
 242 budget time series, with trend significance assessed via a two-tailed t-test. Spatial trends were derived by  
 243 conducting independent regressions at each grid point, with statistically significant results ( $p < 0.05$ )

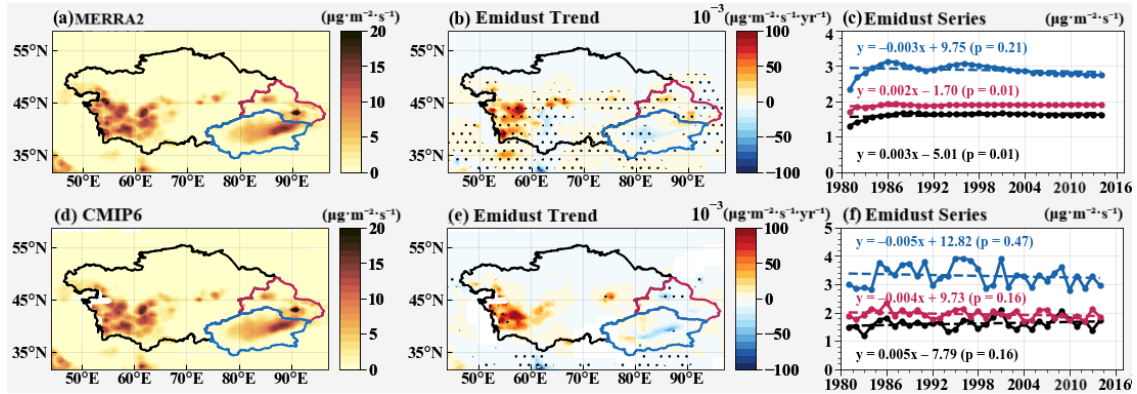
244 indicated by stippling in the figures. Regional mean trends were calculated by regressing the annual  
245 averages of grid values within specific regions (Central Asian countries, northern Xinjiang, and southern  
246 Xinjiang). The regression slopes and corresponding p-values were annotated directly on the time series  
247 plots.

### 248 **3. Results and Analysis**

#### 249 **3.1 Spatial pattern and multi-mode prediction of dust emissions in Central Asia**

250 Figure 2 compares MERRA-2 observations with CMIP6 multi-model ensemble (MME) dust emissions  
251 from 1980 to 2014. The historical spatial distribution from the 10 models is shown in Supplementary  
252 Figure 2. Further analysis indicates that the observations are highly consistent with the MME simulations,  
253 yielding a Taylor skill score (SS) of 0.87 and demonstrating strong performance in both correlation and  
254 standard deviation. Dust emissions in the study area exhibit substantial temporal and spatial variability.  
255 In terms of spatial distribution (Figure 2a), both datasets consistently identify the three primary core  
256 emission sources in the Tarim Basin, the desiccated Aral Sea bed, and the Gobi Desert, with maximum  
257 emission fluxes exceeding  $15 \mu\text{g}\cdot\text{m}^{-2}\cdot\text{s}^{-1}$ . Regarding the trends in dust emissions (Figure 2b), those in  
258 the Aral Sea region have increased significantly ( $>0.5 \mu\text{g}\cdot\text{m}^{-2}\cdot\text{s}^{-1} \text{yr}^{-1}$ ) over the past 34 years, whereas  
259 those in the Tarim Basin have slightly decreased ( $\approx -0.3 \mu\text{g}\cdot\text{m}^{-2}\cdot\text{s}^{-1} \text{yr}^{-1}$ ).

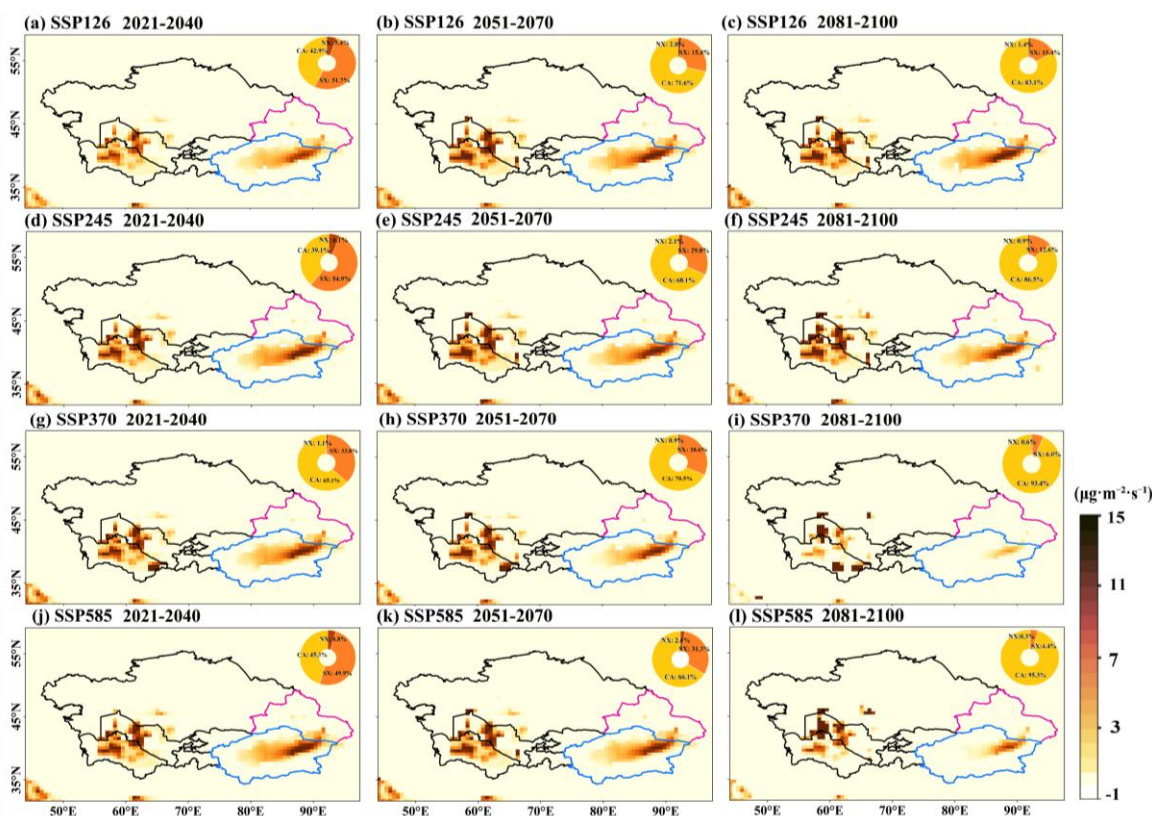
260 The Aral Sea region has experienced a 68% reduction in lake area since 1960, resulting in 54,000 km<sup>2</sup> of  
261 exposed lakebed (Wang et al., 2020). Under arid climatic conditions—with annual average precipitation  
262 of less than 100 mm and potential evaporation exceeding 2000 mm—the dust emission flux has increased  
263 significantly at a rate of approximately  $0.5 \mu\text{g}\cdot\text{m}^{-2}\cdot\text{s}^{-1} \text{yr}^{-1}$  over 34 years. In contrast, the Tarim Basin has  
264 benefited from ecological restoration projects and increased precipitation during the growing season (Fu  
265 et al., 2021), leading to a decrease in emission flux at a rate of  $\approx -0.3 \mu\text{g}\cdot\text{m}^{-2}\cdot\text{s}^{-1} \text{yr}^{-1}$ . Time series analysis  
266 (Figure 2c) shows that overall dust emissions fluctuate gently without significant annual trends. Dust  
267 emissions in the southern Tarim Basin of Xinjiang exhibit annual increases and decreases, consistent  
268 with the spatial trend distribution. Dust emissions in northern Xinjiang are similar to those in Central  
269 Asia, with northern Xinjiang slightly higher than other Central Asian regions. This may be attributed to  
270 local differences in surface roughness and land use, reflecting regional disparities in emission  
271 characteristics.



272 **Figure 2** Spatial distribution, linear trends, and time series of dust emissions from MERRA-2 and  
 273 **the CMIP6 multi-model ensemble (MME) in Central Asia from 1980 to 2014. The red outline**  
 274 **delineates Northern Xinjiang, the blue outline delineate Southern Xinjiang, and the black outlines**  
 275 **denote the five Central Asian countries. Black dots in panels (b) and (e) mark regions significant**  
 276 **at the 95% confidence level.**

277 In the future projections, Figure 3 illustrates the relative changes in dust emissions over Central Asia  
 278 under four radiative forcing scenarios (SSP1-2.6, SSP2-4.5, SSP3-7.0, and SSP5-8.5) for the near term  
 279 (2021–2040), midterm (2051–2070), and long term (2081–2100), relative to the baseline period (1980–  
 280 2014). The results reveal pronounced spatiotemporal heterogeneity in dust emissions across the region  
 281 (absolute values are shown in Supplementary Figure 7). Under all scenarios, regions with high dust  
 282 emission values (changes  $>10 \mu\text{g}\cdot\text{m}^{-2}\cdot\text{s}^{-1}$  and relative change rates  $>25\%$ ) are consistently located in the  
 283 Aral Sea basin, Turkmenistan, and the eastern margin of the Tarim Basin. Overall, dust emission intensity  
 284 shows a positive correlation with the magnitude of radiative forcing and increases progressively over  
 285 time within each scenario (long term  $>$  midterm  $>$  near term). Specifically, in the Aral Sea region, near-  
 286 term dust emissions range from  $17.8 \mu\text{g}\cdot\text{m}^{-2}\cdot\text{s}^{-1}$  (SSP3-7.0) to  $26.0 \mu\text{g}\cdot\text{m}^{-2}\cdot\text{s}^{-1}$  (SSP2-4.5), with relatively  
 287 small inter-scenario differences. However, as radiative forcing intensifies and time progresses, the rate  
 288 of change in emissions rises from approximately 40% in the near term to about 70% in the midterm.  
 289 Under the high-radiative-forcing scenario (SSP5-8.5), the long-term increase reaches its maximum, with  
 290 an enhancement of about 94.9% relative to the reference period. This substantial increase is closely  
 291 associated with the exposure of saline–alkaline sediments from the desiccated lakebed, soil loosening  
 292 due to rising surface temperatures, and intensified wind erosion (Lioubimtseva and Cole, 2006).  
 293 In contrast, the Tarim Basin exhibits an overall decreasing trend in dust emissions, primarily driven by  
 294 the combined effects of ecological restoration (a decadal NDVI increase of 0.12) and enhanced growing-  
 295 season precipitation (Xu et al., 2019). Specifically, dust emissions decline by 18.7% under SSP2-4.5 and

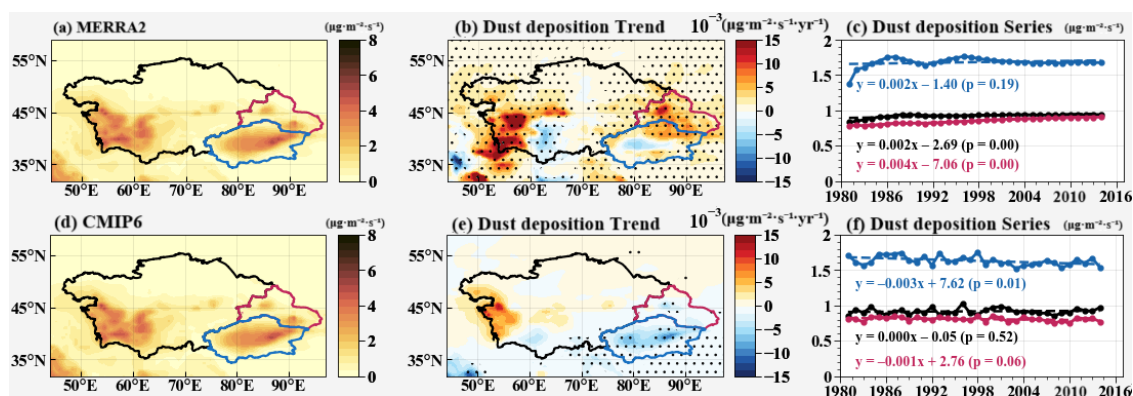
296 by 29.3% under SSP3-7.0. Under the SSP5-8.5 scenario, emissions decrease from  $27.2 \mu\text{g}\cdot\text{m}^{-2}\cdot\text{s}^{-1}$  in the  
 297 near term to  $20.1 \mu\text{g}\cdot\text{m}^{-2}\cdot\text{s}^{-1}$  in the long term, representing a reduction of approximately 26.1%, with the  
 298 relative change rate showing a concurrent weakening trend. A regional comparison reveals substantial  
 299 differences in climate response sensitivity: the emission increases over the Aral Sea region exhibit an  
 300 exponential relationship with radiative forcing intensity ( $R^2 = 0.93$ ), whereas those in southern Xinjiang  
 301 show a slight declining tendency. This contrast highlights the potential role of human interventions in  
 302 modulating dust processes across Central Asia.



303  
 304 **Figure. 3** Future changes in dust emissions across different periods. Spatial distribution of the  
 305 relative changes in dust emissions over Central Asia under four CMIP6 multi-model ensemble  
 306 (MME) SSP scenarios: panels (a–d) near term (2021–2040), (e–h) midterm (2051–2070), and (i–l)  
 307 long term (2081–2100), relative to the historical period (2000–2014). The circular inset in the  
 308 upper-right corner of each panel indicates the mean relative change rate (%) for the corresponding  
 309 region.

310 Dust emissions and deposition together constitute the complete dust mass balance process, with  
 311 deposition representing the ultimate outcome of dust release. Once injected into the atmosphere, dust  
 312 particles undergo dry deposition, driven primarily by gravitational settling, and wet deposition, facilitated  
 313 by precipitation (the historical spatial distributions of dry and wet deposition from the ten models are  
 314 shown in Supplementary Figures 3–4), thereby completing the material redistribution across the land–

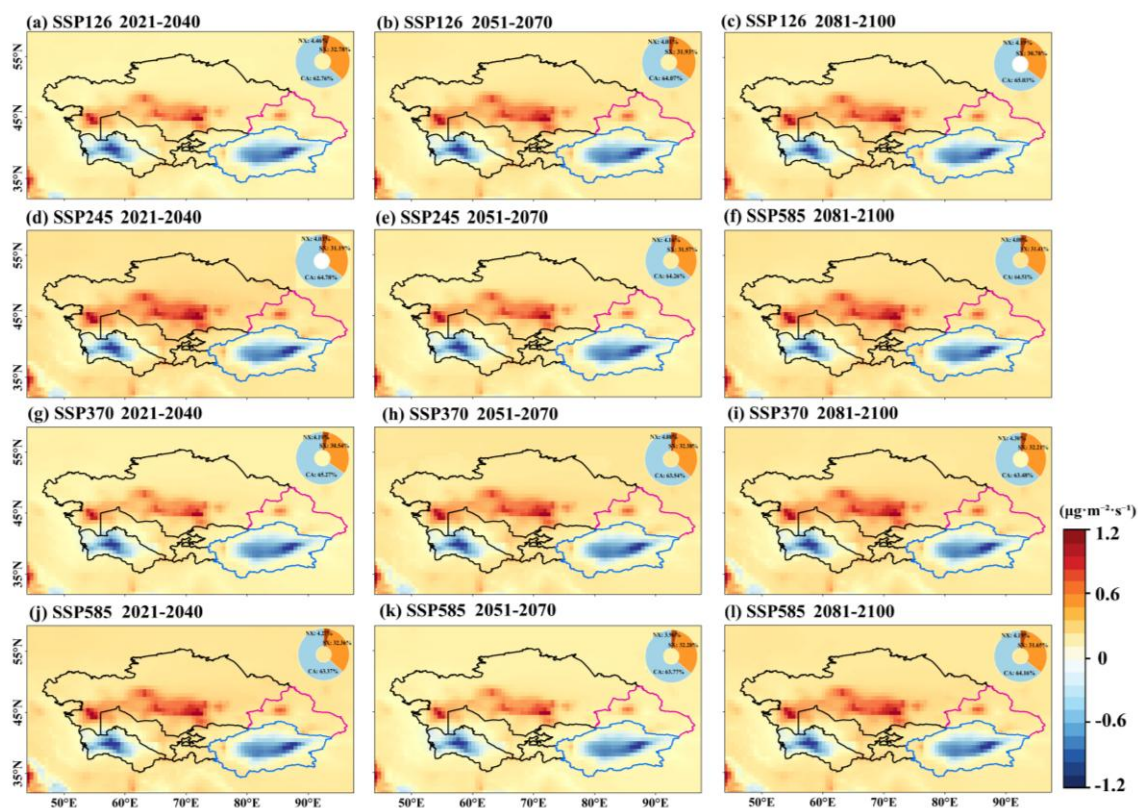
315 atmosphere interface (Marticorena and Bergametti, 1995; Shao et al., 2011). Quantitative assessments  
 316 (Figure 4 and Supplementary Figures 5–6) indicate that the multi-model ensemble (MME) simulations  
 317 agree well with observations in reproducing total dust deposition over Central Asia, yielding a Taylor  
 318 skill score of 0.82. However, differences exist in the absolute magnitudes of deposition, and the observed  
 319 trend intensity from MERRA-2 is substantially stronger than that simulated by the model ensemble.  
 320 Spatially, regions with high deposition ( $>5 \mu\text{g}\cdot\text{m}^{-2}\cdot\text{s}^{-1}$ ) largely coincide with emission hotspots, mainly  
 321 concentrated in western Central Asia and the Tarim Basin in southern Xinjiang, confirming the spatially  
 322 coupled “emission–deposition” mechanism of local dust processes. Trend analysis (Figure 4b) reveals  
 323 that the Aral Sea and the eastern Caspian region exhibit the strongest positive trends ( $\Delta S = +0.15$   
 324  $\mu\text{g}\cdot\text{m}^{-2}\cdot\text{s}^{-1}$ ), whereas southern Xinjiang is dominated by a negative trend ( $\Delta S = -0.10 \mu\text{g}\cdot\text{m}^{-2}\cdot\text{s}^{-1}$ ).  
 325 Temporally (Figure 4c), the observational data show a slight increasing trend in dust deposition flux over  
 326 Central Asia during 1980–2014, with a rate of  $0.002 \mu\text{g}\cdot\text{m}^{-2}\cdot\text{s}^{-1} \text{ yr}^{-1}$ , while the MME simulations indicate  
 327 a weak decreasing trend of  $-0.003 \mu\text{g}\cdot\text{m}^{-2}\cdot\text{s}^{-1} \text{ yr}^{-1}$  over Xinjiang. This discrepancy between observations  
 328 and simulations may stem from uncertainties in model representations of boundary-layer dynamics and  
 329 precipitation microphysics in arid Central Asia, particularly in the quantification of dust wet deposition  
 330 efficiency, which still requires improvement.



331  
 332 **Figure. 4** Spatial distribution, linear trends, and temporal variations of total dust deposition (dry  
 333 + wet) over Central Asia from 1980 to 2014, based on MERRA-2 observations and CMIP6 multi-  
 334 model ensemble (MME) simulations. Red shading highlights northern Xinjiang, blue shading  
 335 indicates southern Xinjiang, and black outlines denote the five Central Asian countries. In panels  
 336 (b) and (e), black dots denote regions where the trends are statistically significant at the 95%  
 337 confidence level ( $p < 0.05$ ).

338 Figure 5 illustrates the projected relative changes in dust deposition ( $\mu\text{g}$ ) under four SSP scenarios across  
 339 different time periods (future changes in dry and wet deposition are shown in Supplementary Figures 9–

340 10). Unlike the source-concentrated distribution of dust emissions, the spatial extent of deposition  
 341 extends outward, mainly covering southwestern Central Asia, the southeastern margin of the Tarim Basin,  
 342 and the Junggar Basin, with maximum deposition fluxes exceeding  $8 \mu\text{g}\cdot\text{m}^{-2}\cdot\text{s}^{-1}$ . This forms a distinct  
 343 spatial pattern characterized by a “deposition domain > emission source.” From a temporal perspective,  
 344 near-term (2021–2040) mean deposition ranges from  $9.3 \mu\text{g}\cdot\text{m}^{-2}\cdot\text{s}^{-1}$  (SSP5-8.5) to  $10.4 \mu\text{g}\cdot\text{m}^{-2}\cdot\text{s}^{-1}$  (SSP2-  
 345 4.5), whereas long-term (2081–2100) values vary between  $9.6 \mu\text{g}\cdot\text{m}^{-2}\cdot\text{s}^{-1}$  (SSP3-7.0) and  $10.0 \mu\text{g}\cdot\text{m}^{-2}\cdot\text{s}^{-1}$   
 346 (SSP1-2.6). The overall change is less than  $1 \mu\text{g}\cdot\text{m}^{-2}\cdot\text{s}^{-1}$ , corresponding to a variation amplitude below  
 347 12%, and the relative change rate remains stable across all scenarios, suggesting that future radiative  
 348 forcing exerts limited influence on dust deposition processes. This phenomenon may be attributed to the  
 349 compensatory effects between dry and wet deposition. In southern Xinjiang, changes in the precipitation  
 350 regime under moderate-to-high radiative forcing lead to a gradual decline in dry deposition flux at a rate  
 351 of approximately  $0.2 \mu\text{g}\cdot\text{m}^{-2}\cdot\text{s}^{-1} \text{ yr}^{-1}$ . Conversely, in western Central Asia, enhanced near-surface wind  
 352 speeds resulting from reduced surface roughness increase dry deposition, while the spatiotemporal  
 353 stability of wet deposition mitigates fluctuations in total deposition.

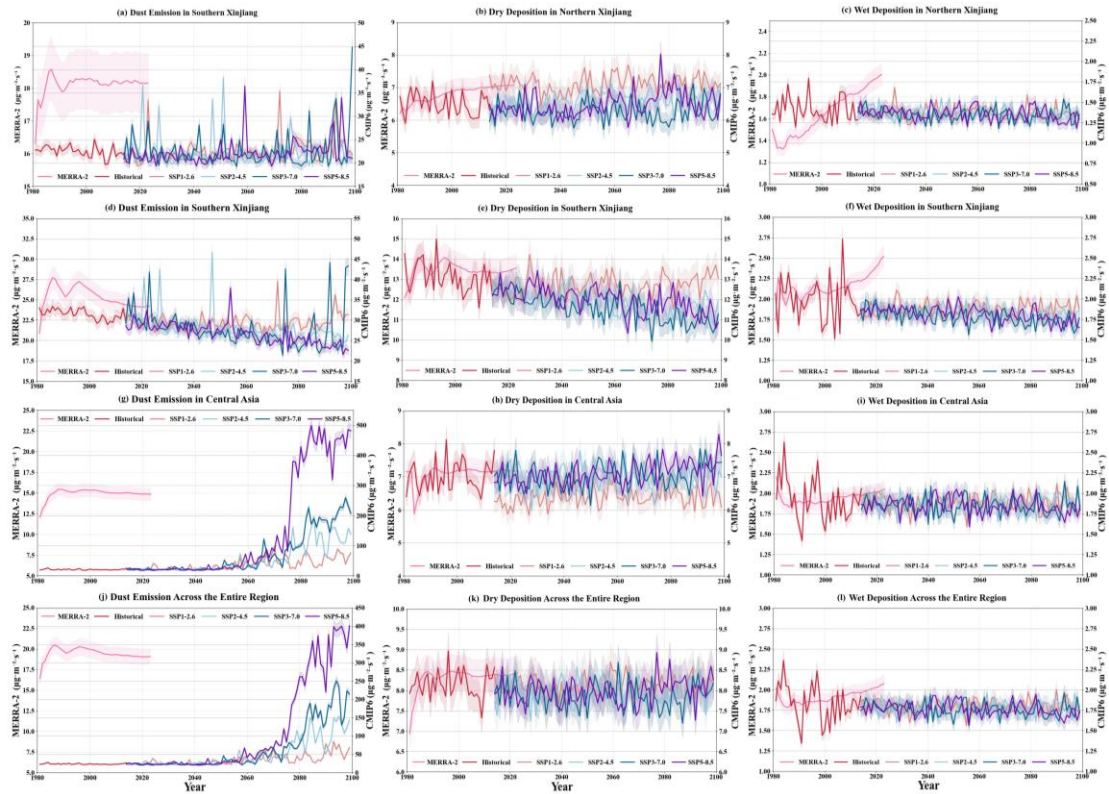


354  
 355 **Figure. 5** Spatial distribution of relative changes in total dust deposition over Central Asia under  
 356 **four CMIP6 multi-model ensemble (MME) SSP scenarios for different future periods: panels (a–**  
 357 **d) near term (2021–2040), (e–h) midterm (2051–2070), and (i–l) long term (2081–2100), relative to**

358 **the historical period (2000–2014). The circular inset in the upper-right corner of each panel**  
359 **indicates the mean relative change rate (%) for the corresponding region.**

360 To more accurately assess the trend simulation performance of the dust cycle, we constructed time series  
361 of dust emissions and wet and dry deposition from 1980 to 2100 based on MERRA-2 reanalysis data and  
362 CMIP6 multi-model ensemble (MME) simulations (see Fig. 6). Overall, the simulations indicate that  
363 dust emissions in Xinjiang remain relatively stable over the next 120 years. In contrast, in the five Central  
364 Asian countries—particularly under high-radiative-forcing scenarios (e.g., SSP3-7.0, SSP5-8.5)—dust  
365 emissions increase significantly (e.g., up to 94.9% under SSP5-8.5) between 2081 and 2100,  
366 accompanied by a fluctuating but gradual rise. By comparison, dust deposition (both dry and wet) exhibits  
367 a smoother trend with lower volatility.

368 In the specific analyses, MERRA-2 dust emissions show a smooth trend, with averages of  $30 \mu\text{g}\cdot\text{m}^{-2}\cdot\text{s}^{-1}$   
369 in the Tarim Basin and  $15 \mu\text{g}\cdot\text{m}^{-2}\cdot\text{s}^{-1}$  in other regions. In contrast, MME-simulated emissions exhibit  
370 slight fluctuations, with peaks exceeding  $45 \mu\text{g}\cdot\text{m}^{-2}\cdot\text{s}^{-1}$  at certain times. Some deviations are observed in  
371 the temporal variability between the two datasets. The volatility of dust dry deposition is relatively low,  
372 with a slope of less than 0.1, indicating a smooth process. Additionally, neither dry nor wet deposition  
373 shows significant long-term volatility. Wet deposition exhibits slight deviations in northern Xinjiang but  
374 remains relatively smooth in other regions, with an average flux of approximately  $1.5 \mu\text{g}\cdot\text{m}^{-2}\cdot\text{s}^{-1}$  and an  
375 overall slope of less than 0.2, indicating limited variation. Notably, MERRA-2 wet deposition data show  
376 a marked increase in the northern border region around 2000, likely related to the assimilation of MODIS  
377 satellite and other observations in MERRA-2. Therefore, MERRA-2 data from 2000 to 2014 were  
378 selected for model calibration to ensure simulation accuracy. In summary, although future dust emissions  
379 vary substantially under different climate scenarios, the overall dust deposition process remains relatively  
380 stable. The MERRA-2 and MME simulation results exhibit spatial and temporal differences across  
381 regions.



382

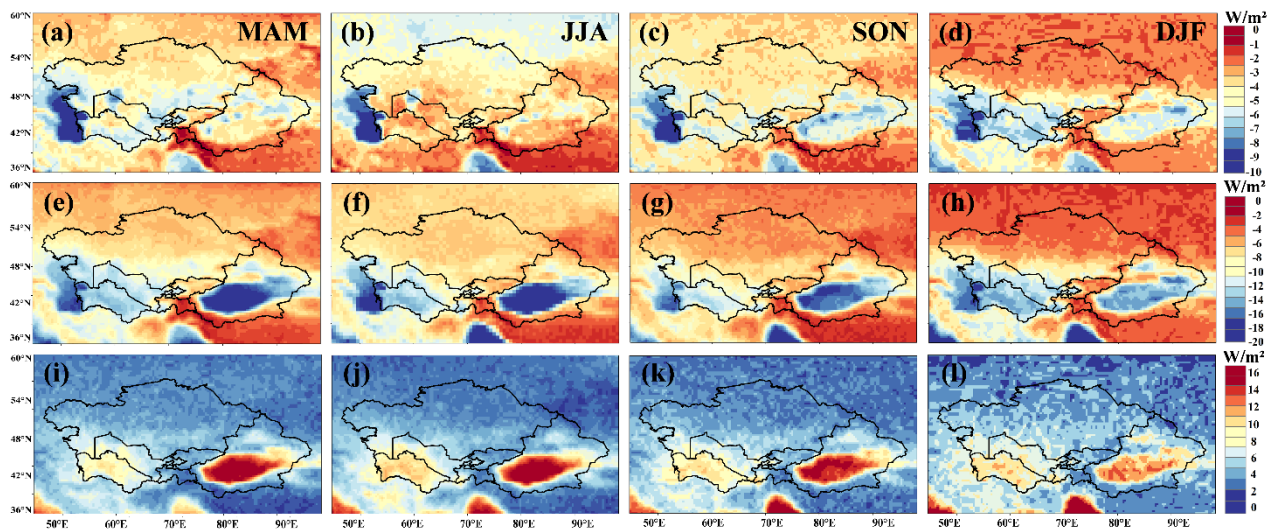
383 **Figure 6.** Time evolution of the dust budget. Dust emissions, dry and wet deposition ( $\mu\text{g}\cdot\text{m}^{-2}\cdot\text{s}^{-1}$ )  
 384 for panels (a–c) Northern Xinjiang, (d–f) Southern Xinjiang, (g–i) Central Asia, and (j–l) the entire  
 385 study region. Results are from the CMIP6 multi-model ensemble (MME; 1980–2100) and  
 386 MERRA-2 (1980–2023).

### 387 3.3.1 Monthly average changes in direct radiative forcing by dust aerosols

388 Based on the quantitative characterization of dust emission sources and deposition processes described  
 389 above, further investigation is needed to elucidate the perturbation mechanisms of dust aerosols on the  
 390 surface–atmosphere energy balance. This study quantifies the radiative impacts of Central Asian dust  
 391 aerosols at various spatial and temporal scales through shortwave aerosol direct radiative forcing (ADRF)  
 392 derived from MERRA-2 observations under clear-sky conditions from 1980 to 2023. As shown in Figure  
 393 7a–d, the top-of-atmosphere (TOA) radiative forcing exhibits substantial spatial heterogeneity. Overall,  
 394 the negative forcing reaches its lowest values ( $<-10\text{ W/m}^2$ ) in the Caspian Sea region, followed by the  
 395 Tarim Basin and the Aral Sea region ( $<-8\text{ W/m}^2$ ), confirming that dust aerosols exert a significant cooling  
 396 effect by enhancing shortwave reflection. Seasonal analysis reveals that the negative TOA forcing  
 397 intensity decreases in the order spring ( $-3.32\text{ W/m}^2$ ) > summer ( $-3.21\text{ W/m}^2$ ) > autumn ( $-3.07\text{ W/m}^2$ ) >  
 398 winter ( $-1.94\text{ W/m}^2$ ), which aligns closely with the seasonal characteristics of dust activity. In spring,  
 399 strong surface wind erosion across Central Asia drives intense dust emissions, resulting in high

400 atmospheric dust loading and optical depth and, consequently, the strongest radiative forcing. Although  
 401 summer convective activity can transport dust to higher altitudes, weakened near-surface wind erosion  
 402 reduces the overall dust burden relative to spring(Ginoux et al. 2012). During autumn and winter, dust  
 403 activity declines markedly, yielding the weakest annual radiative forcing.

404 The spatial pattern of surface (SFC) radiative forcing (Figure 7e–h) exhibits stronger negative values,  
 405 with two pronounced cooling centers over the Tarim Basin and southwestern Central Asia, where  
 406 shortwave radiation loss peaks at  $-20 \text{ W/m}^2$ . This arises from the combined scattering and absorption  
 407 effects of dust particles on incoming solar radiation (Li et al., 2022a), which substantially reduce surface  
 408 net radiation, thereby diminishing sensible heat flux and evaporation processes and suppressing the  
 409 transfer of heat and water vapor from the surface to the atmosphere. The atmospheric radiative forcing  
 410 (ADRF) exhibits a spatial pattern consistent with those at the TOA and SFC but features positive values  
 411 ( $10.02 \text{ W/m}^2$  in spring and  $9.89 \text{ W/m}^2$  in summer), indicating the energy redistribution role of dust  
 412 aerosols in trapping solar energy within the atmospheric system via shortwave absorption. This vertical  
 413 gradient of “surface cooling and atmospheric heating” induces substantial changes in the regional  
 414 thermodynamic structure(Kok et al. 2017). On one hand, surface cooling diminishes sensible heat flux  
 415 and evaporation, thereby exacerbating moisture deficits in Central Asia's arid regions and limiting  
 416 vegetation growth and agricultural productivity. On the other hand, atmospheric heating strengthens the  
 417 temperature gradient from the boundary layer to the free troposphere, enhancing the potential for deep  
 418 convection, which could intensify the frequency and severity of spring–summer dust storms and modify  
 419 regional precipitation patterns and extreme weather events.



420 **Figure. 7 Seasonal spatial distribution of clear-sky shortwave aerosol direct radiative forcing**  
421 **(ADRF) due to dust aerosols in Central Asia (1980–2023): at the top of the atmosphere (panels a–**  
422 **d), at the surface (e–h), and in the atmosphere (i–l).**

### 423 **3.3.2 Refinement of aerosol direct radiative forcing in dusty weather**

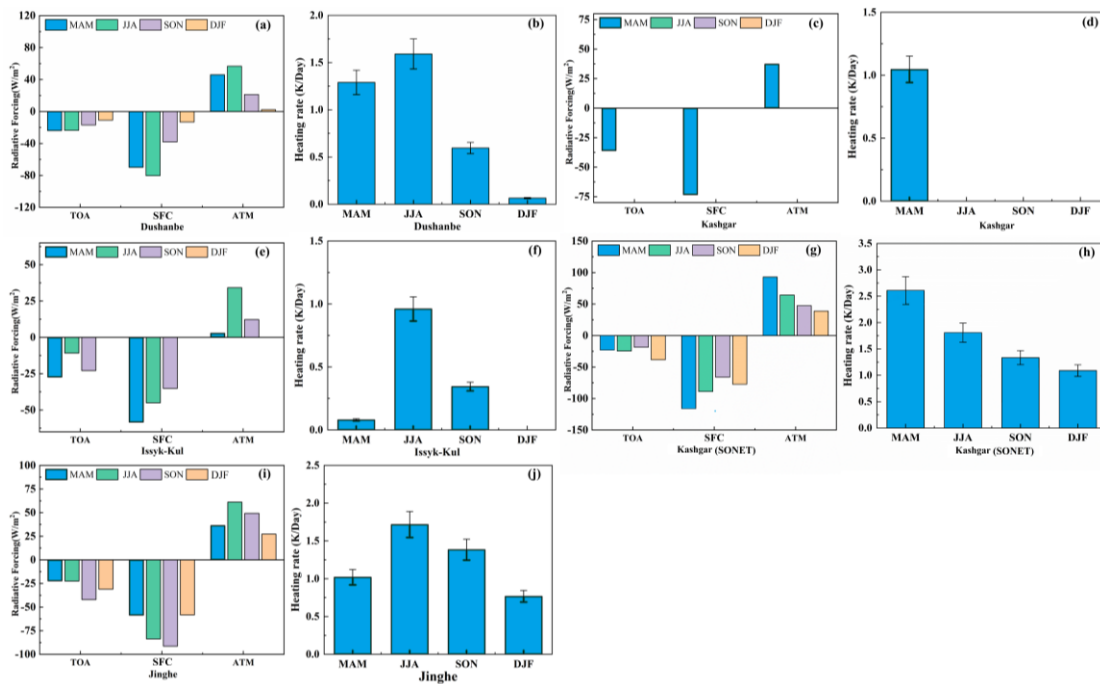
424 Following a thorough examination of the spatial distribution characteristics of atmospheric dust aerosol  
425 direct radiative forcing (DRF) derived from MERRA-2 reanalysis data, this study further refines the  
426 analysis by simulating the radiative effects of dust aerosols at representative Central Asian sites using  
427 the Santa Barbara DISORT Atmospheric Radiative Transfer (SBDART) model (Figure 8).

428 These simulations are based on ground-based observations from 2011 to 2023, encompassing AERONET  
429 sites at Dushanbe (Tajikistan; representing the Central Asian interior), Issyk-Kul (Kyrgyzstan;  
430 representing high-altitude lake regions), and Kashgar (Xinjiang, China; representing the Tarim Basin  
431 dust source region), as well as the SONET site at Kashgar and our self-established Jinghe site (Xinjiang,  
432 China; representing the Gobi–desert transitional zone). Although the number of sites is limited, their  
433 spatial distribution covers the primary dust source regions and representative surface types, thereby  
434 achieving a degree of regional representativeness. This section focuses on site-scale aerosol direct  
435 radiative forcing (ADRF), with particular emphasis on atmospheric radiative forcing (ATM) and the  
436 associated atmospheric heating rates, to provide a detailed understanding of the thermodynamic effects  
437 of dust on the atmospheric column.

438 Observations indicate that ADRF exhibits distinct seasonal variations. At the Dushanbe, Issyk-Kul, and  
439 Jinghe sites, atmospheric radiative forcing peaks in summer (56.72, 34.22, and 61.17 W/m<sup>2</sup>, respectively)  
440 and declines to annual minima in winter (approximately 2.33 W/m<sup>2</sup> at Dushanbe and 27.36 W/m<sup>2</sup> at  
441 Jinghe), consistent with the frequent summer dust events in western Central Asia driven by westerly  
442 circulation (Li et al., 2022b). Notably, the Kashgar site exhibits a unique spring-dominated pattern, with  
443 a maximum ADRF of 92.99 W/m<sup>2</sup>, which may be associated with the Tarim Basin’s specific dust  
444 emission mechanisms, involving springtime snowmelt that exposes bare surfaces and interacts with  
445 intense Mongolian cyclone activity.

446 Changes in the atmospheric heating rate maintain a clear positive correlation with ADRF, confirming the  
447 central role of radiation absorption by dust aerosols. The peaks in heating rates at all sites occur during  
448 the active dust period: those at Dushanbe (1.29 K/day in summer) and Jinghe (1.72 K/day in summer)  
449 align with westerly transport paths, while the anomalously high value at Kashgar in spring (2.61 K/day)

450 corresponds to significant sand uplift events in the Taklamakan Desert. Notably, the heating rate at Issyk-  
 451 Kul in spring (0.08 K/day) is substantially lower than that in autumn (0.34 K/day), possibly due to the  
 452 site being shielded by mountainous terrain, which limits vertical dust transport in spring. This may also  
 453 affect the accuracy of the results, given the relative scarcity of observational data at the Issyk-Kul  
 454 site. This study reveals that the spatial and temporal divergence of regional radiative effects is primarily  
 455 controlled by two major factors: (1) seasonal modulation of emission intensity in dust source regions,  
 456 exemplified by enhanced ATM dust transport from westerly jets to the Aral Sea basin in summer, and (2)  
 457 modulation of localized atmospheric boundary layer processes, typically manifested as differences in  
 458 thermal response between a mountainous site (Issyk-Kul) and a basin site (Kashgar). These findings  
 459 provide essential observational constraints for improving dust-radiation parameterization schemes in  
 460 regional climate models.

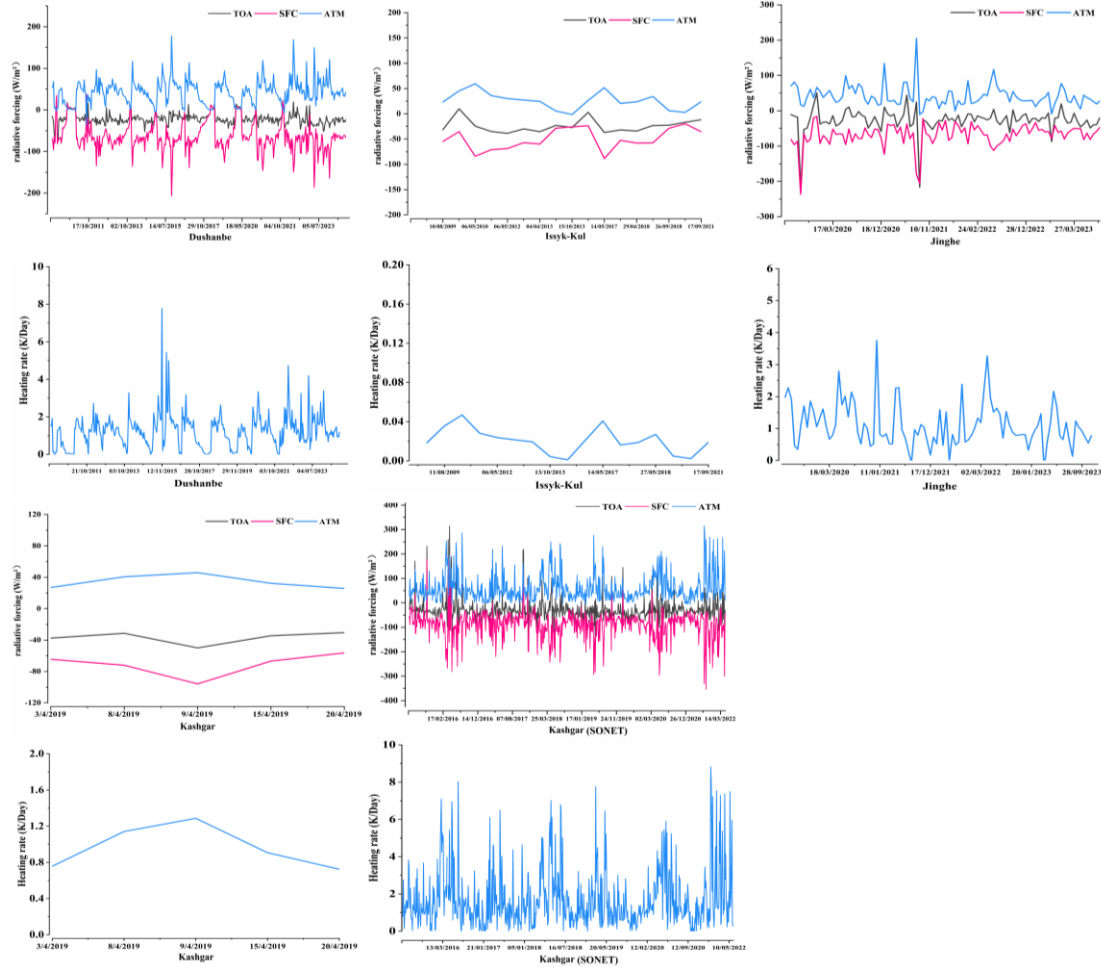


461  
 462 **Figure 8** Seasonally averaged shortwave radiative forcing and atmospheric heating rate (including  
 463 direct radiative forcing at the top of the atmosphere (TOA), the surface (SUR), and the atmosphere  
 464 (ATM)) for dust aerosols at stations in Central Asia.

465 Figure 9 provides a further refinement of the aerosol direct radiative forcing (ADRF) at the sites,  
 466 revealing that the daily variations in radiative forcing at the top of the atmosphere (TOA), surface (SFC),  
 467 and throughout the atmosphere exhibit a clear pattern of temporal divergence. The ADRF time series at  
 468 each site shows a differentiated response: at Dushanbe (2011–2023), typical characteristics of inland  
 469 Central Asia are evident, with TOA and SFC forcing oscillating within  $\pm 200$  W/m<sup>2</sup> and atmospheric

470 heating rates peaking at 8 K/day. Short-term variations are primarily driven by intermittent dust transport  
471 induced by disturbances in the westerly jet. At the Jinghe site, a generally stable trend is observed,  
472 punctuated by transient episodes of strong negative forcing ( $SFC < -250W/m^2$ ) during extreme dust  
473 events. The Kashgar site displays pronounced temporal variability, with TOA/SFC forcing ranging from  
474  $\pm 400 W/m^2$  and heating rates between 0 and 8 K/day during 2016–2022, including high-frequency  
475 oscillations in the afternoons of spring and summer. This behavior is directly linked to the Tarim Basin’s  
476 unique “afternoon mixed-layer development–vertical dust uplift” mechanism (Nakamae and Takemi,  
477 2022), which may further increase the likelihood of regional dust events by intensifying local convective  
478 activity.

479 Notably, recent observations indicate enhanced irregular variability in ADRF during 2020–2023, which  
480 may be attributed to the combined effects of changing surface cover and the increased frequency of  
481 extreme weather events in arid Central Asia, resulting in heightened instability in dust emissions and  
482 boundary-layer thermodynamic responses. At Kashgar, pronounced day-to-day fluctuations ( $\Delta ADRF >$   
483  $50 W/m^2$ ) reveal the sensitive feedback of aerosol loading from the Taklamakan Desert source region on  
484 boundary-layer thermodynamics. These high-resolution observational results suggest that transient  
485 perturbations in dust radiative effects may alter boundary-layer stability and convective potential, thereby  
486 influencing precipitation variability and ecosystem stability in arid Central Asia. Such findings provide  
487 critical observational constraints for dust–radiation parameterizations in regional climate models.



488

489 **Figure. 9** Shortwave direct radiative forcing and atmospheric heating rates at Central Asian sites  
 490 (AERONET/SONET data). Upper panels (a, b, c, g, h) show forcing at the top of the atmosphere  
 491 (TOA), surface (SFC), and in the atmosphere (ATM); lower panels (d, e, f, i, j) show the  
 492 corresponding atmospheric heating rates for (a, d) Dushanbe, (b, e) Issyk-Kul, (c, f) Jinghe, and  
 493 (g–j) Kashgar.

494 **4. Conclusion and discussion**

495 **4.1 Conclusion**

496 Dust aerosols play a pivotal role in the climate system, characterized by substantial complexity and  
 497 regional variability. This study compares the spatial distributions and temporal trends of dust emissions  
 498 and deposition in Central Asia, while projecting future trends based on MERRA-2 reanalysis data and  
 499 dust cycle simulations from the CMIP6 multi-model ensemble (MME). Comparative analysis from 1980  
 500 to 2014 reveals strong consistency between the reanalysis data and MME simulations. The primary dust  
 501 emission hotspots are the Tarim Basin, the desiccated Aral Sea region, and the Gobi Desert, where  
 502 maximum emission fluxes exceed  $15 \mu\text{g} \cdot \text{m}^{-2} \cdot \text{s}^{-1}$ . Over the 34-year period, dust emissions in the Aral Sea

503 region have increased significantly ( $>0.5 \mu\text{g}\cdot\text{m}^{-2}\cdot\text{s}^{-1}\cdot\text{yr}^{-1}$ ), whereas emission fluxes in the Tarim Basin  
504 exhibit a declining trend at a rate of  $\approx -0.3 \mu\text{g}\cdot\text{m}^{-2}\cdot\text{s}^{-1}\cdot\text{yr}^{-1}$ .

505 Regarding short-, medium-, and long-term projections, regions with high dust emission values in Central  
506 Asia remain stable in the Aral Sea hinterland, Turkmenistan, and along the eastern margin of the Tarim  
507 Basin. Short-term emissions in the Aral Sea region range from 17.8 to 26.0  $\mu\text{g}\cdot\text{m}^{-2}\cdot\text{s}^{-1}$ , exhibiting  
508 minimal inter-scenario variation; however, under high-radiative-forcing scenarios (e.g., SSP5-8.5), long-  
509 term dust emissions in Central Asia increase to 387.1  $\mu\text{g}\cdot\text{m}^{-2}\cdot\text{s}^{-1}$ , representing an enhancement of up to  
510 94.9% relative to the reference period. In contrast, long-term emissions in the Tarim Basin demonstrate  
511 a declining trend, with reductions ranging from 18.7% under the SSP2-4.5 scenario to 29.3% under the  
512 SSP3-7.0 scenario. Particularly under the SSP5-8.5 scenario, short-term emissions stand at 27.2  
513  $\mu\text{g}\cdot\text{m}^{-2}\cdot\text{s}^{-1}$ , decreasing to 20.1  $\mu\text{g}\cdot\text{m}^{-2}\cdot\text{s}^{-1}$  in the long term—a reduction of 26.1%.

514 Regions with high dust deposition values ( $>5 \mu\text{g}\cdot\text{m}^{-2}\cdot\text{s}^{-1}$ ) overlap substantially with emission hotspots.  
515 Trend analysis reveals that the Aral Sea and the eastern Caspian region exhibit the strongest positive  
516 trends ( $\Delta S = +0.15 \mu\text{g}\cdot\text{m}^{-2}\cdot\text{s}^{-1}$ ), whereas southern Xinjiang shows a negative trend ( $\Delta S = -0.10$   
517  $\mu\text{g}\cdot\text{m}^{-2}\cdot\text{s}^{-1}$ ). Under the four future scenarios, dust deposition influences extend across southwestern  
518 Central Asia, the southeastern margin of the Tarim Basin, and the Junggar Basin, with maximum fluxes  
519 exceeding 8  $\mu\text{g}\cdot\text{m}^{-2}\cdot\text{s}^{-1}$ . Mean values in the near term (2021–2040) range from 9.3  $\mu\text{g}\cdot\text{m}^{-2}\cdot\text{s}^{-1}$  (SSP5-8.5)  
520 to 10.4  $\mu\text{g}\cdot\text{m}^{-2}\cdot\text{s}^{-1}$  (SSP2-4.5), and from 9.6  $\mu\text{g}\cdot\text{m}^{-2}\cdot\text{s}^{-1}$  (SSP3-7.0) to 10.0  $\mu\text{g}\cdot\text{m}^{-2}\cdot\text{s}^{-1}$  (SSP1-2.6) in the  
521 long term (2081–2100), with an overall variation of less than 12%.

522 The aerosol direct radiative forcing (ADRF) due to dust aerosols under clear skies in Central Asia exhibits  
523 notable spatial patterns. Overall, the top-of-atmosphere (TOA) radiative forcing is negative, with the  
524 lowest values observed in the Caspian Sea region ( $<-10 \text{ W/m}^2$ ), followed by the Tarim Basin and the Aral  
525 Sea region ( $<-8 \text{ W/m}^2$ ). The seasonal TOA forcing minima decrease in the order spring ( $-3.32 \text{ W/m}^2$ ) >  
526 summer ( $-3.21 \text{ W/m}^2$ ) > autumn ( $-3.07 \text{ W/m}^2$ ) > winter ( $-1.94 \text{ W/m}^2$ ). At the surface (SFC), radiative  
527 forcing reaches a peak of  $-20 \text{ W/m}^2$  in the Tarim Basin and southwestern Central Asia. Atmospheric  
528 shortwave radiative forcing aligns spatially with TOA and SFC patterns, peaking at  $10.02 \text{ W/m}^2$  in spring,  
529 which correlates closely with the seasonal characteristics of dust activity.

530 Simulations using the SBDART model indicate that aerosol direct radiative forcing (ADRF) at the sites  
531 peaks in summer at Dushanbe ( $56.72 \text{ W/m}^2$ ), Issyk-Kul ( $34.22 \text{ W/m}^2$ ), and Jinghe ( $61.17 \text{ W/m}^2$ ),

532 declining to annual minima in winter (approximately 2.33 W/m<sup>2</sup> at Dushanbe and 27.36 W/m<sup>2</sup> at Jinghe).  
533 At Kashgar, ADRF exhibits a distinct spring peak of 92.99 W/m<sup>2</sup>. Variations in atmospheric heating rates  
534 show a strong positive correlation with ADRF. Heating rate peaks occur during the active dust season at  
535 all sites: summer at Dushanbe (1.29 K/day) and Jinghe (1.72 K/day), and spring at Kashgar (2.61 K/day).  
536 Notably, the heating rate at Issyk-Kul is substantially lower in spring (0.08 K/day) than in autumn (0.34  
537 K/day), reflecting seasonal modulation of dust emission intensity and the influence of local boundary  
538 layer processes.

## 539 **4.2 Discussion**

### 540 **4.2.1 SARIMA Forecasting**

541 This study integrates MERRA-2 reanalysis data, CMIP6 multi-model ensemble (MME) simulations, and  
542 ground-based sun photometer observations to develop a fully coupled “emission–deposition–radiation”  
543 framework for the dust cycle in Central Asia, thereby systematically elucidating the radiative regulatory  
544 mechanisms of dust aerosols on the land–atmosphere system. To address the pronounced spatiotemporal  
545 heterogeneity in aerosol radiative forcing and the limitations of observational data, this study employs a  
546 seasonal autoregressive integrated moving average (SARIMA) model. Leveraging MERRA-2 reanalysis  
547 data and SBDART-derived site-level radiative forcing time series from 1980 to 2023, this approach  
548 facilitates short-term predictive analyses from local to regional scales.

549 In contrast to century-scale CMIP6 scenario simulations, the SARIMA model quantifies the interannual  
550 and short-term internal variability in dust radiative forcing (Kumar et al. 2018), enabling operational  
551 forecasts for the next 5–10 years. This method is particularly well-suited for near-term predictions of  
552 high-uncertainty variables, as it effectively captures seasonal and short-term fluctuations while providing  
553 quantitative support for regional dust risk assessments and policy formulation. Methodologically, it  
554 complements long-term model simulations by providing a near-term predictive perspective (Mondal et al.  
555 2025, Sami et al. 2012).

556 The forecast results (Figure 10) indicate that dust radiative forcing over the arid regions of Central Asia  
557 during 2024–2029 exhibits an overall quasi-stationary pattern, with interannual fluctuations ranging from  
558 1.6 to 9.8 W/m<sup>2</sup> (peaking in 2026) and no indications of extreme events. Regional differences are  
559 pronounced: southern Xinjiang represents a strong radiative response zone (2.8–18.9 W/m<sup>2</sup>), whereas  
560 northern Xinjiang shows a non-stationary trend of initial increase followed by decline (1.6–10.0 W/m<sup>2</sup>),

561 likely reflecting the bidirectional modulation of dust emissions by changes in snow cover.

562 Model validation results (Supplementary Figure 11) confirm that the residuals of the

563 SARIMA(1,1,0)×(1,0,2)<sub>12</sub> model satisfy the white noise assumption (Ljung–Box Q test,  $p > 0.05$ ) and

564 approximate normality (Kolmogorov–Smirnov test,  $D = 0.12$ ), with autocorrelation coefficients falling

565 within the 95% confidence interval. Quantitative metrics of predictive performance include RMSE =

566 1.72 W/m<sup>2</sup>, MAE = 1.21 W/m<sup>2</sup>, MAPE = 8.6%, and  $R^2 = 0.70$ , demonstrating the model’s strong

567 capability for short-term predictions.

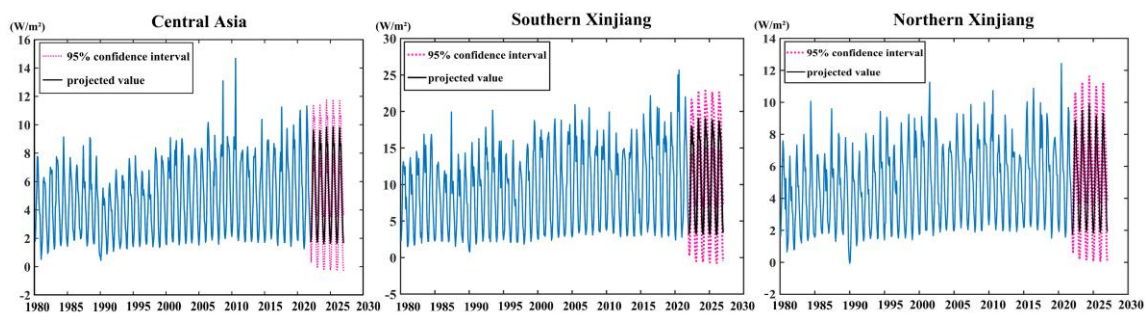
568 Thus, the SARIMA model serves as a methodological complement: it not only validates the internal

569 variability captured in reanalysis and observational time series but also provides operational forecasts for

570 near-future regional climate risk management. This short-term predictive approach complements CMIP6

571 long-term simulations, bridging the gap between large-scale climate projections and near-term adaptation

572 needs.



573

574 **Figure.10 Dust aerosol direct radiative forcing SARIMA model predictions.**

575 **4.2.2 Uncertainty Analysis**

576 The CMIP6 multi-model ensemble (MME) provides a robust analytical framework for assessing future

577 variations in dust budgets across Central Asia. However, differences among models in dust emission

578 parameterization, particle size distribution, and surface schemes introduce a degree of uncertainty in the

579 simulations. To systematically evaluate these uncertainties and enhance the reliability of the results, this

580 study employs complementary diagnostic approaches that quantify both inter-model variability and

581 biases arising from the statistical downscaling procedure.

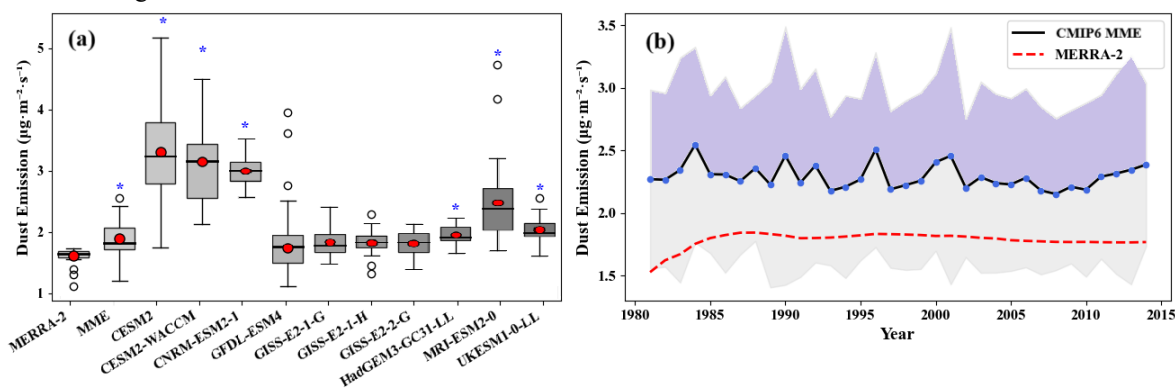
582 To assess inter-model dispersion, dust emissions from each model were compared with MERRA-2

583 reanalysis data(Onyutha et al. 2016). As shown in Figure 10a, emission biases of individual models were

584 evaluated using a two-tailed t-test ( $p < 0.05$ ) to determine statistical significance. The results indicate

585 that several models—including CESM2, CESM2-WACCM, CNRM-ESM2-1, and MRI-ESM2-1—

586 exhibit relatively large deviations, suggesting that their dust modules or physical parameterization  
 587 schemes may introduce additional uncertainties. Figure 10b further illustrates the time series of dust  
 588 emissions along with the  $\pm 1\sigma$  inter-model variability (shaded area). Despite the dispersion among models,  
 589 the MERRA-2 record consistently falls within the historical model range, indicating that the MME  
 590 ensemble mean provides a reasonable representation of the climatological mean state and effectively  
 591 captures the “three-source, high-emission” spatial pattern characteristic of Central Asia’s major dust  
 592 source regions.

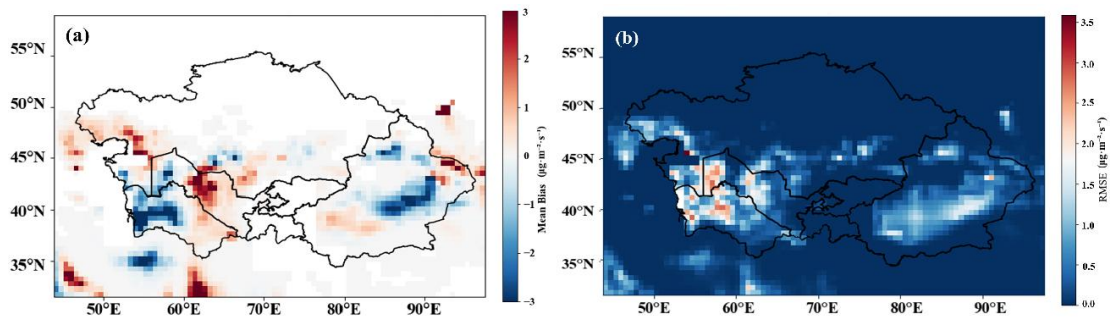


593 **Figure. 11 (a) Dust emission biases of individual models relative to MERRA-2 reanalysis data; (b)**  
 594 **time series of dust emissions from the CMIP6 multi-model ensemble, with  $\pm 1\sigma$  inter-model**  
 595 **variability indicated by the shaded area.**

596 To further elucidate regional differences, Figure 11a and Supplementary Figure 12 depict the spatial bias  
 597 distributions of individual models within the multi-model ensemble (MME). The results reveal that all  
 598 models exhibit biases in key dust source regions, including the Taklamakan Desert, Kumtag Desert, areas  
 599 surrounding the Aral Sea, Karakum Desert, and the eastern Caspian Sea. Specifically, positive biases  
 600 predominate in the southeastern Tarim Basin, whereas negative biases dominate in the western Karakum  
 601 Desert and parts of the Aral Sea region.

602 The bias-corrected statistical downscaling method employed in this study, which relies on MERRA-2  
 603 data, is well-suited to Central Asia's complex terrain and sparse observational networks. It offers low  
 604 computational costs while preserving the statistical relationships between dust emissions and climate  
 605 variables. However, its capacity to simulate extreme events and nonlinear processes (e.g., intense dust  
 606 storms) remains limited. To quantify downscaling biases, Figure 12b illustrates the spatial root-mean-  
 607 square error (RMSE) between CMIP6 downscaled outputs and MERRA-2 data. The results indicate  
 608 higher RMSE values ( $>2 \mu\text{g}\cdot\text{m}^{-2}\cdot\text{s}^{-1}$ ) in complex terrain regions, such as the Tarim Basin and Karakum  
 609 Desert, suggesting that predictions in these areas should be interpreted with caution. Supplementary

610 Figure 13 presents a scatterplot demonstrating a high correlation between downscaled MME changes ( $\Delta$   
 611 MME) and MERRA-2 observations ( $R^2 > 0.91$ ), although a slight underestimation bias is evident (Bias  
 612 =  $-1.26$ , RMSE =  $4.31$ ). The time series comparison in Supplementary Figure 13b further demonstrates  
 613 that the downscaled results effectively capture seasonal and interannual variability. Overall, the multi-  
 614 model ensemble, combined with bias-corrected downscaling, demonstrates reasonable robustness,  
 615 providing a credible reference for assessing future dust changes in Central Asia.



616  
 617 **Figure. 12 (a) Spatial distribution of biases between individual models in the multi-model ensemble**  
 618 **and MERRA-2 reanalysis data; (b) spatial distribution of root-mean-square error (RMSE)**  
 619 **between CMIP6 downscaled outputs and MERRA-2 reanalysis data.**

620 Although the results presented above provide multiple lines of evidence for understanding the dust cycle  
 621 in Central Asia, their limitations cannot be overlooked. The dust budget encompasses key processes such  
 622 as emission, transport, deposition, and mass loading. While previous studies have advanced our  
 623 knowledge, achieving a comprehensive understanding of the complex interactions among dust, land  
 624 surface, vegetation, and climate remains a significant challenge. In particular, variability in dust particle  
 625 size assumptions across CMIP6 models markedly affects simulation consistency (Zhao, Ryder and  
 626 Wilcox 2022), thereby increasing uncertainty in representing dust cycle processes.

627 Second, although existing radiative transfer models such as SBDART are suitable for point-scale  
 628 simulations, they do not fully account for aerosol–cloud interactions, which are particularly important in  
 629 regions with high dust concentrations; neglecting this process may introduce biases in radiative forcing  
 630 estimates. The SBDART simulations in this study rely on a limited set of ground-based observational  
 631 sites in Central Asia, which, while representative in terms of geographic location and underlying surface  
 632 types, are sparsely distributed and thus capture only local responses at typical sites rather than spatially  
 633 averaged effects across the entire region. For example, the Ili Lake site exhibits lower atmospheric  
 634 heating rates in spring, likely attributable to data scarcity and the shielding effects of complex  
 635 mountainous terrain, underscoring the challenges of high-altitude observations.

636 Due to the sparse observational network, no weighting was applied to the sites; instead, they were treated  
637 as independent case studies to highlight variability under different environmental conditions. The  
638 representativeness of these sites is corroborated by cross-validation with MERRA-2 reanalysis data  
639 (Supplementary Figure 1); however, they still cannot fully characterize the complex radiative effects  
640 across Central Asia's extensive and heterogeneous landscapes.

#### 641 **Author contributions**

642 All authors contributed to the manuscript and approved the final version. YG designed the study,  
643 performed the data analysis, and wrote the original draft. WC, JD, and YR assisted with data collection  
644 and software processing. YR also contributed to the validation and interpretation of results. ZZ  
645 supervised the research and contributed to manuscript revision and funding acquisition.

#### 646 **Competing interests.**

647 The contact author has declared that none of the authors has any competing interests.

#### 648 **Funding**

649 Open Project of Key Laboratory in Xinjiang Uygur Autonomous Region of China (2023D04066),  
650 National Natural Science Foundation of China (No. 42061066), and Xinjiang University Outstanding  
651 Graduate Student Innovation Program(XJDX2025YJS065).

#### 652 **Acknowledgements**

653 We are sincerely grateful to MERRA-2 (<https://gmao.gsfc.nasa.gov/reanalysis/MERRA-2/>), CMIP6  
654 (<https://esgf-node.ipsl.upmc.fr/projects/cmip6-ipsl/>), AERONET and SONET Instrument Science  
655 Teams for providing the datasets, which are available on the Web and constitute the centralized  
656 database for the current work. We thank the faculty members who worked hard to review this thesis.

#### 657 **References:**

658 Braconnot, P., S. Albani, Y. Balkanski, A. Cozic, M. Kageyama, A. Sima, O. Marti & J.-Y.  
659 Peterschmitt (2021) Impact of dust in PMIP-CMIP6 mid-Holocene simulations with the IPSL model.

660 Climate of the Past, 17, 1091-1117.

661 Brown, H., X. Liu, R. Pokhrel, S. Murphy, Z. Lu, R. Saleh, T. Mielonen, H. Kokkola, T. Bergman  
662 & G. Myhre (2021) Biomass burning aerosols in most climate models are too absorbing. Nature  
663 communications, 12, 277.

664 Buchard, V., C. Randles, A. Da Silva, A. Darmenov, P. Colarco, R. Govindaraju, R. Ferrare, J. Hair,  
665 A. Beyersdorf & L. Ziemba (2017) The MERRA-2 aerosol reanalysis, 1980 onward. Part II:  
666 Evaluation and case studies. Journal of climate, 30, 6851-6872.

667 Chen, A., C. Zhao & T. Fan (2022) Spatio-temporal distribution of aerosol direct radiative forcing  
668 over mid-latitude regions in north hemisphere estimated from satellite observations. Atmospheric  
669 Research, 266, 105938.

670 Dai, Y., P. Hitchcock, N. M. Mahowald, D. I. Domeisen, D. S. Hamilton, L. Li, B. Marticorena, M.  
671 Kanakidou, N. Mihalopoulos & A. Aboagy-Okyere (2022) Stratospheric impacts on dust transport  
672 and air pollution in West Africa and the Eastern Mediterranean. Nature Communications, 13, 7744.

673 Dubovik, O. & M. D. King (2000) A flexible inversion algorithm for retrieval of aerosol optical  
674 properties from Sun and sky radiance measurements. Journal of Geophysical Research:  
675 Atmospheres, 105, 20673-20696.

676 Eyring, V., S. Bony, G. A. Meehl, C. A. Senior, B. Stevens, R. J. Stouffer & K. E. Taylor (2016)  
677 Overview of the Coupled Model Intercomparison Project Phase 6 (CMIP6) experimental design and  
678 organization. Geoscientific Model Development, 9, 1937-1958.

679 Fu, A., W. Li, Y. Chen, Y. Wang, H. Hao, Y. Li, F. Sun, H. Zhou, C. Zhu & X. Hao (2021) The effects  
680 of ecological rehabilitation projects on the resilience of an extremely drought-prone desert riparian  
681 forest ecosystem in the Tarim River Basin, Xinjiang, China. Scientific Reports, 11, 18485.

682 García, O., J. Díaz, F. Expósito, A. Díaz, O. Dubovik, Y. Derimian, P. Dubuisson & J.-C. Roger  
683 (2012) Shortwave radiative forcing and efficiency of key aerosol types using AERONET data.  
684 Atmospheric Chemistry and Physics, 12, 5129-5145.

685 Gelaro, R., W. McCarty, M. J. Suárez, R. Todling, A. Molod, L. Takacs, C. A. Randles, A. Darmenov,  
686 M. G. Bosilovich & R. Reichle (2017) The modern-era retrospective analysis for research and  
687 applications, version 2 (MERRA-2). Journal of climate, 30, 5419-5454.

688 Gutmann, E., T. Pruitt, M. P. Clark, L. Brekke, J. R. Arnold, D. A. Raff & R. M. Rasmussen (2014)

689 An intercomparison of statistical downscaling methods used for water resource assessments in the  
690 United States. *Water Resources Research*, 50, 7167-7186.

691 Halthore, R. N., D. Crisp, S. E. Schwartz, G. Anderson, A. Berk, B. Bonnel, O. Boucher, F. L. Chang,  
692 M. D. Chou & E. E. Clothiaux (2005) Intercomparison of shortwave radiative transfer codes and  
693 measurements. *Journal of Geophysical Research: Atmospheres*, 110.

694 Heald, C., D. Ridley, J. Kroll, S. Barrett, K. Cady-Pereira, M. Alvarado & C. Holmes (2014)  
695 Contrasting the direct radiative effect and direct radiative forcing of aerosols. *Atmospheric  
696 Chemistry and Physics*, 14, 5513-5527.

697 Hetzel, R., S. Niedermann, M. Tao, P. W. Kubik, S. Ivy-Ochs, B. Gao & M. R. Strecker (2002) Low  
698 slip rates and long-term preservation of geomorphic features in Central Asia. *Nature*, 417, 428-432.

699 Holben, B. N., T. F. Eck, I. a. Slutsker, D. Tanre, J. Buis, A. Setzer, E. Vermote, J. A. Reagan, Y.  
700 Kaufman & T. Nakajima (1998) AERONET—A federated instrument network and data archive for  
701 aerosol characterization. *Remote sensing of environment*, 66, 1-16.

702 Holben, B. N., D. Tanré, A. Smirnov, T. Eck, I. Slutsker, N. Abuhassan, W. Newcomb, J. Schafer,  
703 B. Chatenet & F. Lavenu (2001) An emerging ground-based aerosol climatology: Aerosol optical  
704 depth from AERONET. *Journal of Geophysical Research: Atmospheres*, 106, 12067-12097.

705 Kok, J. F., T. Storelvmo, V. A. Karydis, A. A. Adebisi, N. M. Mahowald, A. T. Evan, C. He & D. M.  
706 Leung (2023) Mineral dust aerosol impacts on global climate and climate change. *Nature Reviews  
707 Earth & Environment*, 4, 71-86.

708 Li, J., B. E. Carlson, Y. L. Yung, D. Lv, J. Hansen, J. E. Penner, H. Liao, V. Ramaswamy, R. A. Kahn  
709 & P. Zhang (2022a) Scattering and absorbing aerosols in the climate system. *Nature Reviews Earth  
710 & Environment*, 3, 363-379.

711 Li, X., Y. Liu, M. Wang, Y. Jiang & X. Dong (2021) Assessment of the Coupled Model  
712 Intercomparison Project phase 6 (CMIP6) Model performance in simulating the spatial-temporal  
713 variation of aerosol optical depth over Eastern Central China. *Atmospheric Research*, 261, 105747.

714 Li, Y., Y. Song, D. G. Kaskaoutis, X. Zhang, X. Chen, N. Shukurov & R. Orozbaev (2022b)  
715 Atmospheric dust dynamics over Central Asia: A perspective view from loess deposits. *Gondwana  
716 Research*, 109, 150-165.

717 Li, Z., H. Xu, K. Li, D. Li, Y. Xie, L. Li, Y. Zhang, X. Gu, W. Zhao & Q. Tian (2018) Comprehensive

718 study of optical, physical, chemical, and radiative properties of total columnar atmospheric aerosols  
719 over China: An overview of Sun–Sky Radiometer Observation Network (SONET) measurements.  
720 *Bulletin of the American Meteorological Society*, 99, 739-755.

721 Lioubimtseva, E. & R. Cole (2006) Uncertainties of climate change in arid environments of Central  
722 Asia. *Reviews in Fisheries Science*, 14, 29-49.

723 Liu, J., X. Wang, D. Wu, H. Wei, Y. Li & M. Ji (2024) Historical footprints and future projections  
724 of global dust burden from bias-corrected CMIP6 models. *npj Climate and Atmospheric Science*, 7,  
725 1.

726 Mahowald, N. M., S. Kloster, S. Engelstaedter, J. K. Moore, S. Mukhopadhyay, J. R. McConnell, S.  
727 Albani, S. C. Doney, A. Bhattacharya, M. A. J. Curran, M. G. Flanner, F. M. Hoffman, D. M.  
728 Lawrence, K. Lindsay, P. A. Mayewski, J. Neff, D. Rothenberg, E. Thomas, P. E. Thornton & C. S.  
729 Zender (2010) Observed 20th century desert dust variability: impact on climate and biogeochemistry.  
730 *Atmos. Chem. Phys.*, 10, 10875-10893.

731 Maraun, D., F. Wetterhall, A. Ireson, R. Chandler, E. Kendon, M. Widmann, S. Brienen, H. Rust, T.  
732 Sauter & M. Themeßl (2010) Precipitation downscaling under climate change: Recent  
733 developments to bridge the gap between dynamical models and the end user. *Reviews of geophysics*,  
734 48.

735 Marticorena, B. & G. Bergametti (1995) Modeling the atmospheric dust cycle: 1. Design of a soil-  
736 derived dust emission scheme. *Journal of geophysical research: atmospheres*, 100, 16415-16430.

737 Nakamae, K. & T. Takemi (2022) Relationship between the development of a convective mixed  
738 layer and dust weather in arid and semi-arid regions of East Asia. *International Journal of*  
739 *Climatology*, 42, 3076-3093.

740 Penner, J. E., J. Quaas, T. Storelvmo, T. Takemura, O. Boucher, H. Guo, A. Kirkevåg, J. E.  
741 Kristjánsson & Ø. Seland (2006) Model intercomparison of indirect aerosol effects. *Atmospheric*  
742 *Chemistry and Physics*, 6, 3391-3405.

743 Pozzer, A., A. De Meij, K. Pringle, H. Tost, U. Doering, J. Van Aardenne & J. Lelieveld (2012)  
744 Distributions and regional budgets of aerosols and their precursors simulated with the EMAC  
745 chemistry-climate model. *Atmospheric Chemistry and Physics*, 12, 961-987.

746 Ramanathan, V., P. J. Crutzen, J. Kiehl & D. Rosenfeld (2001) Aerosols, climate, and the

747 hydrological cycle. *science*, 294, 2119-2124.

748 Ricchiazzi, P., S. Yang, C. Gautier & D. Sowle (1998) SBDART: A research and teaching software  
749 tool for plane-parallel radiative transfer in the Earth's atmosphere. *Bulletin of the American*  
750 *Meteorological Society*, 79, 2101-2114.

751 Salvador, P., J. Pey, N. Pérez, X. Querol & B. Artíñano (2022) Increasing atmospheric dust transport  
752 towards the western Mediterranean over 1948–2020. *NPJ Climate and Atmospheric Science*, 5, 34.

753 Shao, Y., K.-H. Wyrwoll, A. Chappell, J. Huang, Z. Lin, G. H. McTainsh, M. Mikami, T. Y. Tanaka,  
754 X. Wang & S. Yoon (2011) Dust cycle: An emerging core theme in Earth system science. *Aeolian*  
755 *Research*, 2, 181-204.

756 She, L., Z. Li, G. de Leeuw, W. Wang, Y. Wang, L. Yang, Z. Feng, C. Yang & Y. Shi (2024) Time  
757 series retrieval of Multi-wavelength Aerosol optical depth by adapting Transformer (TMAT) using  
758 Himawari-8 AHI data. *Remote Sensing of Environment*, 305, 114115.

759 Shen, H., J. Abuduwaili, A. Samat & L. Ma (2016) A review on the research of modern aeolian dust  
760 in Central Asia. *Arabian Journal of Geosciences*, 9, 1-16.

761 Sirisha, U. M., M. C. Belavagi & G. Attigeri (2022) Profit prediction using ARIMA, SARIMA and  
762 LSTM models in time series forecasting: A comparison. *IEEE Access*, 10, 124715-124727.

763 Sokolik, I. N. & O. B. Toon (1996) Direct radiative forcing by anthropogenic airborne mineral  
764 aerosols. *Nature*, 381, 681-683.

765 Song, Q., Z. Zhang, H. Yu, P. Ginoux & J. Shen (2021) Global dust optical depth climatology  
766 derived from CALIOP and MODIS aerosol retrievals on decadal timescales: regional and  
767 interannual variability. *Atmospheric Chemistry and Physics*, 21, 13369-13395.

768 Tanaka, T. Y. & M. Chiba (2006) A numerical study of the contributions of dust source regions to  
769 the global dust budget. *Global and Planetary Change*, 52, 88-104.

770 Tao, M., L. Chen, J. Wang, L. Wang, W. Wang, C. Lin, L. Gui, L. Wang, C. Yu & Y. Wang (2022)  
771 Characterization of dust activation and their prevailing transport over East Asia based on multi-  
772 satellite observations. *Atmospheric research*, 265, 105886.

773 Tegen, I., M. Werner, S. Harrison & K. E. Kohfeld (2004) Relative importance of climate and land  
774 use in determining present and future global soil dust emission. *Geophysical research letters*, 31.

775 Wallace, J. M. & P. V. Hobbs. 2006. *Atmospheric science: an introductory survey*. Elsevier.

776 Wang, X., Y. Chen, Z. Li, G. Fang, F. Wang & H. Liu (2020) The impact of climate change and  
777 human activities on the Aral Sea Basin over the past 50 years. *Atmospheric Research*, 245, 105125.  
778 Wang, X., J. Liu, H. Che, F. Ji & J. Liu (2018) Spatial and temporal evolution of natural and  
779 anthropogenic dust events over northern China. *Scientific Reports*, 8, 2141.  
780 Wang, Z., L. Lin, Y. Xu, H. Che, X. Zhang, H. Zhang, W. Dong, C. Wang, K. Gui & B. Xie (2021)  
781 Incorrect Asian aerosols affecting the attribution and projection of regional climate change in  
782 CMIP6 models. *npj Climate and Atmospheric Science*, 4, 2.  
783 Wu, T. & B. E. Boor (2021) Urban aerosol size distributions: a global perspective. *Atmospheric*  
784 *Chemistry and Physics*, 21, 8883-8914.  
785 Xu, M., X. Wang, T. Sun, H. Wu, X. Li & S. Kang (2019) Water balance change and its implications  
786 to vegetation in the Tarim River Basin, Central Asia. *Quaternary International*, 523, 25-36.  
787 Zhang, X.-X., C. Claiborn, J.-Q. Lei, J. Vaughan, S.-X. Wu, S.-Y. Li, L.-Y. Liu, Z.-F. Wang, Y.-D.  
788 Wang & S.-Y. Huang (2020) Aeolian dust in Central Asia: Spatial distribution and temporal  
789 variability. *Atmospheric Environment*, 238, 117734.  
790 Zhao, A., C. L. Ryder & L. J. Wilcox (2022) How well do the CMIP6 models simulate dust aerosols?  
791 *Atmospheric Chemistry and Physics*, 22, 2095-2119.  
792 Zhao, A., L. J. Wilcox & C. L. Ryder (2024) The key role of atmospheric absorption in the Asian  
793 summer monsoon response to dust emissions in CMIP6 models. *Atmospheric Chemistry and*  
794 *Physics*, 24, 13385-13402.  
795 Zhao, Y., X. Yue, Y. Cao, J. Zhu, C. Tian, H. Zhou, Y. Chen, Y. Hu, W. Fu & X. Zhao (2023) Multi-  
796 model ensemble projection of the global dust cycle by the end of 21st century using the Coupled  
797 Model Intercomparison Project version 6 data. *Atmos. Chem. Phys.*, 23, 7823-7838.  
798